3D Finite Element Model for Predicting Cutting Forces in Machining Unidirectional Carbon Fiber Reinforced Polymer (CFRP) Composites

by

Amir Salar Salehi
B.Sc., Azad University of Mashhad, 2008

A Thesis Submitted in Partial Fulfillment
of the Requirements for the Degree of

MASTER OF APPLIED SCIENCE

in the Department of Mechanical Engineering

Supervisory Committee

3D Finite Element Model for Predicting Cutting Forces in Machining Unidirectional Carbon Fiber Reinforced Polymer (CFRP) Composites

by

Amir Salar Salehi
B.Sc., Azad University of Mashhad, 2008

Supervisory Committee

Dr. Martin Byung-Guk Jun – Department of Mechanical Engineering
Co-Supervisor

Dr. Keivan Ahmadi – Department of Mechanical Engineering
Co-Supervisor

Abstract

Supervisory Committee
Dr. Martin Byung-Guk Jun, Department of Mechanical Engineering
Co-Supervisor
Dr. Keivan Ahmadi, Department of Mechanical Engineering
Co-Supervisor

Excellent properties of Carbon Fiber Reinforced Polymer (CFRP) composites are usually obtained in the direction at which carbon fibers are embedded in the polymeric matrix material. The outstanding properties of this material such as high strength to weight ratio, high stiffness and high resistance to corrosion can be tailored to meet specific design applications. Despite their excellent mechanical properties, application of CFRPs has been limited to more lucrative sectors such as aerospace and automotive industries. This is mainly due to the high costs involved in manufacturing of this material. Machining, milling and drilling, is a critical part of finishing stage of manufacturing process. Milling and drilling of CFRP is complicated due to the inhomogeneous nature of the material and extreme abrasiveness of carbon fibers. This is why CFRP parts are usually made near net shape. However, no matter how close they are produced to the final shape, there still is an inevitable need for some post machining to obtain dimensional accuracies and tolerances. Problems such as fiber-matrix debonding, subsurface damage, rapid tool wear, matrix cracking, fiber pull-out, and delamination are usually expected to occur in machining CFRPs. These problems can affect the dimensional accuracy and performance of the CFRP part in its future application.

To improve the efficiency of the machining processes, i.e. to reduce the costs and increase the surface quality, researchers began studying machining Fiber Reinforced Polymer (FRP) composites. Studies into FRPs can be divided in three realms; analytical, experimental and numerical. Analytical models are only good for a limited range [0° – 75°] of Fiber Orientations[1], to be found from now on as "FO" in this thesis. Experimental studies are expensive and time consuming. Also, a wide variety of controlling parameters exist in an experimental machining study; including cutting parameters such as depth of cut, cutting speed, FO, spindle speed, feed rate as well as tool geometry parameters such as rake angle, clearance angle, and tool edge/nose radius. Furthermore, the powdery dust created during machining is known to cause serious health hazards for the operator. Numerical models, on the other hand, offer the unique capability of studying the complex interaction between the tool and workpiece as well as chip formation mechanisms during the cut. Large number of contributing parameters can be included in the numerical model without wasting material. Three main objectives of numerical models are to predict principal cutting force, thrust force and post-machining subsurface damage. Knowing these, one can work on optimization of machining process by tool geometry and path design.

[1] Fiber orientation is the clockwise angle between the cutting direction and fiber axis.

Previous numerical studies mainly focus on the orthogonal cutting of FRP composites. Thus, the existing models in the literature are two-dimensional (2D) for the most part. The 2D finite element models assume plain stress or strain condition. Accordingly, the reported results cannot be reliable and extendable to real cutting situations such as drilling and milling, where oblique cutting of the material occurs. Most of the numerical studies to date claim to predict the principle cutting forces fairly acceptable, yet not for the whole range of fiber orientations. Predicted thrust forces, on the other hand, are generally not in good agreement with experimental results at all. Subsurface damage is reported by some experimental studies and again only for a limited FO range. To address the lack of reliable force and subsurface damage prediction model for the whole FO range, this thesis aims to develop a 3D finite element model, in hope of capturing out-of-plane displacements during stress formation in different material phases (Fiber, Matrix and the Interface bonding). ABAQUS software was chosen as the most commonly used finite element simulation tool in the literature.

The present work is completed in three phases. The focus of phase I is to develop a VUMAT program to simulate behavior of carbon fibers during the cut. Carbon fibers are assumed to behave transversely isotropic with brittle (perfectly elastic) fracture. In phase II, elasto-plastic behavior of Epoxy matrix is simulated. Ductile and shear damage models are also incorporated for the matrix. The last phase is to combine the carbon fiber and epoxy matrix phases along with the interface bonding between them. Surface-based cohesive zone technique in ABAQUS is used to simulate the behavior of the zero-thickness bonding layer. The tool is modeled as a rigid body. Mechanical properties were extracted from the literature. The obtained numerical results are compared to the experimental and numerical data in literature. The model is capable of capturing principal forces very well. Cutting force increases with FO from zero to 45° and then decreases up to 135°. The simulated thrust forces are still underestimated mainly due to the fiber elastic recovery effect. Also, the developed 3D model is shown to capture the subsurface damage generally by means of a predefined dimensionless state variable called, Contact Damage (CSDMG). This variable varies between zero and one. It is stored at each time step and can be called out at the end of the analysis. It was shown that depth of fiber-matrix debonding increases with increase in FO.

Table of Contents

List of Tables

List of Figures

Acknowledgments

I would like to take advantage of the opportunity here to gratefully thank my supervisory committee, Dr. Jun and Dr. Ahmadi for being such great mentors to me and providing critical guidelines during the completion of this M.ASC thesis. Also, my wife, Maryam Bidari, for her continued love and support in the many ups and downs we encountered in the course of this study. Deserving a special mention is Mr. Shahram Dindarlou, who was a tremendous help for me, especially with his technical command in writing and debugging the user-defined material subroutine for the present finite element model.

I also wish to express my sincerest gratitude to my friends, Dr. Pejman Azarsa, Dr. Vahid Ahsani, Dr. Ramtin Rakhsha, Dr. Vahid Moradi, Mr. Bardia Sanati, for all their support and assistance and for playing a significant role in accomplishment of the objectives of my work. The last but not the least, I would like to acknowledge my parents, brother and sister for their ever-growing love and encouragement not only in the present work but also in every aspect of my life.

Amir Salar Salehi
University of Victoria
November 2018

Chapter 1 – Introduction

1.1 Overview

Carbon Fiber Reinforced Polymer (CFRP) composites are made of carbon fibers embedded in a polymeric matrix material such as epoxy or resin. The outstanding properties of this material, such as specific strength, high stiffness, high resistance to corrosion can be tailored to meet specific design requirements. Despite their excellent mechanical properties, application of CFRP has been limited to more lucrative sectors such as aerospace, automotive and military industries. This is most probably due to the high manufacturing costs. The constituents, especially carbon fibers, are expensive and special equipment and expertise are required to perform manufacturing processes. Machining of CFRP is complicated due to the inhomogeneous nature of the material and extreme abrasiveness of carbon fibers. This is why CFRP components are usually made near net shape. However, no matter how close to the final shape they are produced, there still exists an inevitable need for some post machining to obtain dimensional accuracies and specified tolerances. Problems such as fiber-matrix debonding, subsurface damage, rapid tool wear, matrix cracking, fiber pull-out, and delamination are usually expected to occur in machining CFRPs, some of which can be seen in Figure 1. These problems can affect the dimensional accuracy and performance of the CFRP part in future applications.

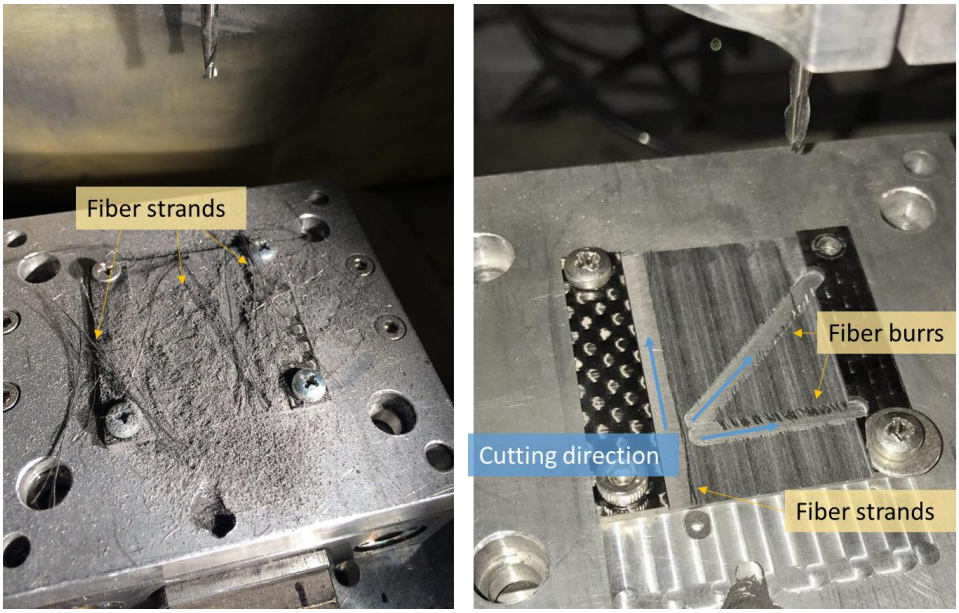

Figure 1 - fiber strands/bur during machining of CFRP laminate

To improve the efficiency of the machining processes, i.e. to reduce the costs and increase the surface quality, researchers began studying the machining process of Fiber Reinforced Polymer (FRP) composites. The main driving force behind this was to understand the complex interaction between the anisotropic inhomogeneous material and the tool as well as to predict the cutting forces and post-machined surface morphology. Studies into FRPs can be divided in three realms; analytical, experimental and numerical. Analytical models are only good for a limited range [0° – 75°] of FOs. Experimental

studies are expensive and time consuming. Also, a wide variety of controlling parameters are involved in an experimental machining study; including cutting parameters such as depth of cut, cutting speed, FO, spindle speed, feed rate as well as tool geometry parameters such as rake angle, clearance angle, and tool edge/nose radius. The powdery dust created during machining may cause serious health problems for the operator. It is also electrically conductive and if it gets inside the electrical components may cause damage due to the short circuit.

Numerical models, on the other hand, offer the unique capability of studying the complex deformation and chip formation mechanisms during the cut. Composites have been numerically investigated at three different constituent levels; micro, macro and meso. In the micro scale, the constituents are studied as separate phases. Usually, three phases exist in a micro-scale finite element model; Fiber, Matrix and the Interface bonding between the two. Consequently, three dissimilar sets of mechanical properties are involved. Interactions between separate phases are usually simulated by defining contact properties and enforcement algorithms. Although micro-scale models can provide excellent information on local effects such as deformation in each phase and surface morphology after cut, they are usually computationally very expensive. Micro-scale simulations usually take a lot of time due to the high number of increments required per analysis step. Elements are usually distorted excessively and the mesh needs to be redefined during analysis. In the macro scale, both fiber and matrix properties are combined to achieve the properties of an Equivalent Homogeneous Anisotropic Material (EHAM). Properties of EHAM are obviously stronger in the direction of fibers. The macro-scale models are computationally more efficient but are not able to capture the local effects such as matrix cracking, fiber-matrix debonding and fiber breakage. Thus, the macro-scale results may not be as accurate as those of micro scale. The third scale introduced to numerical studies as the “meso” scale. This is a combination of the micro and macro scales and takes advantages of both. Adjacent to the tool, the fiber, matrix and their interface are modeled separately and farther away from the tool an EHAM material is usually modeled to save the computational time and provide enough stiffness behind the microscale material. It should be noted here that in the late 2017, one and half years after the start of this thesis, a 3D finite element model was developed by Abena et al. [1] which was simply an extrusion of their previously released 2D model [2]. In this work, carbon fibers were modeled rectangular and not embedded into the matrix material. Although principal cutting forces in their model agreed with experimental results, the thrust forces were still not compliant. Their main focus was based on development of a novel approach to model the cohesive zone (interface) between fiber and matrix.

1.2 Research Motivation

Previous numerical studies vastly deal with orthogonal cutting of FRP composites. Thus, the existing models in the literature are two-dimensional (2D) for the most part. Generally, three main objectives of a numerical model are predicting 1) principal cutting force, 2) thrust force and 3) subsurface damage. Knowing these parameters, one can work on optimization of machining process via tool geometry and path design. The 2D finite element models usually assume a plain stress or strain condition. Accordingly, the reported results cannot be reliable and extendable to real cutting situations such as

drilling and milling, where oblique cutting of the material happens. Most of the numerical studies to date, predict the principle cutting forces to a fairly acceptable extend, yet not for the whole range of fiber orientations, mainly for FOs between 0° to 90°. Predicted thrust forces in the literature are generally not in good agreement with experimental results at all and the subsurface damage is again predicted for only a limited FO range. It should be noted that more work has been done to date on Glass Fiber Reinforced Polymer (GFRP) material rather than CFRP.

To address the lack of reliable force prediction model, both principal and thrust, and subsurface damage during machining of CFRP components for the whole FO range, this thesis aims to develop a 3D finite element model, in hope of capturing out-of-plane displacements during stress formation in different material phases (Fiber, Matrix and Interface). ABAQUS software was chosen as the most commonly used finite element simulation tool in the literature and exceptional capabilities for modeling the interface and complex contact enforcement algorithms. The VUMAT subroutine programming option in ABAQUS enables the user to define any constitutive behavior for the material of interest.

1.3 Research methodology

After comprehensive review on the available literature for numerical modeling of FRP cutting process, this thesis follows three phases. The focus of phase I is to develop a VUMAT program to simulate behavior of carbon fibers during the cut. Carbon fibers are assumed to behave transversely isotropic with brittle (perfectly elastic) fracture to maintain compliance with experimental data. Phase II of the thesis involves Epoxy matrix behavior simulation. Epoxy is considered as an elastic-plastic material. The last phase is to combine the carbon fiber and epoxy matrix phases along with the interface bonding between them. Surface-based cohesive zone modeling is used to simulate the behavior of the zero-thickness bonding layer. Three modes of crack propagation can be defined for the interface, namely normal, shear and tear. However, independent damage modes are chosen in this thesis. The tool is modeled as a rigid body because the elastic modulus of carbide tool is greatly bigger than those of fiber and matrix. Mechanical properties of the EHAM are extracted from the experimental data in literature. No failure model is used for the EHAM as it is positioned well away from the tool.

The numerical results obtained from completion of phase III of this work are compared to the experimental [3] and numerical data [1], [2] in literature. The average deviation from experimental results for principal cutting forces is about 13%. The predicted trend of the thrust force agrees with experimental data. However, the uncertainty in the simulated thrust force results is high. The developed 3D model also captures the subsurface damage generally by means of a predefined state variable called Contact Damage factor, CSDMG. Depth of fiber matrix debonding is defined as the subsurface damage. Due to lack of experimental data in literature, validation of the subsurface damage results remains incomplete.

1.4 Carbon Fiber Reinforced Polymer

1.4.1 Constituents

Composites are generally considered as inhomogeneous and anisotropic materials. They consist of two or more phases. Usually fibers are embedded in the matrix material for reinforcement purposes - to bear the loads. Matrix usually is a softer material and plays the role of transferring the loads to the reinforcement. Also, it protects the fiber from hostile environmental conditions Historically, early composite applications go back to when humans mixed straw and sticks with clay to obtain a lighter and stronger material as a replacement for brick. In nature, wood can be considered as a composite material consisting of strong cellulose fibers held together by a lignin matrix. Bones are another example of natural composite materials having collagen fibers embedded in a mineral matrix. Mechanical properties of the composite material depend on the mechanical properties of its constituents. [4]

1.4.2 Matrix

Polymer matrices have poorer mechanical properties than their metal alloy rivals especially at elevated temperatures. The polymeric matrices are generally either thermoplastics or thermosets. The difference is in the intermolecular bonds between hydrogen and carbon. In thermoplastics, hydrogen molecules are joined to carbon molecules by secondary (Van der Walls) bonds. Since the secondary bond is weaker than the primary (Covalent) bond, thermoplastics easily melt at higher temperatures and reshape. Arrangement of the molecules after cooling might be amorphous (random) or semi-crystalline (regular pattern). Primary bonds between hydrocarbon molecules in thermosets result in less ductile, stiffer and stronger structure than thermoplastics. This polymer cannot be melted easily by simple heating. Instead, when heated enough the material will disintegrate and may ignite. [4]

1.4.3 Fiber

Carbon fibers are the load-bearing component of CFRPs. The shape, volume and direction of the carbon fibers significantly influences the properties of the composite material. Carbon fibers may be long (continuous), short (discontinuous, aligned/random) or particles staggered through the matrix material. Uni-Directional (UD) composites consist of continuous fibers in one direction laid down on the polymeric matrix. Fibers are usually small in diameter, in the range of 7–20 μm. Thousands of fibers form a tow (or yarn or strand). Yarns are put together to form a roving. Carbon fiber properties are highly sensitive to the angle between the graphite layers and the fiber axis. Graphite layers are based on hexagonal rings of carbon with strong covalent bond between atoms. These graphite layers are held on each other by secondary bond, which provides slip along the hexagonal planes. This explains why graphite fibers are much stronger in the longitudinal direction than in the transverse. Carbon fibers are transversely isotropic. This means they possess much stronger properties in the fiber axis direction than the transverse direction. Carbon fibers have two major disadvantages while being manufactured. First, they are highly conductive of electricity. The dust during machining for example may reach machine tool controls and cause short circuit. The dust is also abrasive and can cause chronic diseases for the operator [4].

1.4.4 Manufacturing Processes

Fiber yarns and roving are used in filament winding and pultrusion processes. Tows can be used in pre-impregnation manufacturing process. In this process, fibers are impregnated inside the polymer matrix. Unidirectional prepreg tapes are usually partially-cured and have a variety of applications. They can be used as plies (lamina). These plies are stacked up on top of each other to form a laminate. The final laminate may be uni or multi directional depending on the relative angle between the stacked plies to each other. They can be used to reinforce construction materials such as concrete or be molded (hand-layup) into desired shapes and then fully cured inside an autoclave. Continuous fibers can also be used similar to textile fabrics. Longitudinal fibrous yarn is called warp while the transverse direction yarn is called weft or fill. The crimp is defined as the bending of a fiber when it passes above perpendicular fiber. Woven fabrics may be high or low crimp. Lower crimp leads to more flexibility while a high crimp fabric is generally stiffer [4].

1.4.5 Conventional naming of multidirectional laminates

Multidirectional laminates are produced by the stacking-up the lamina (plies) in different directions. Conventional naming of the multidirectional laminates includes the angles and number of plies used. For example, $[0/45_2/90/90/45_2/0]$ is a laminate consisting of one (0°), two (45°), one (90°), one (90°), two (45°) and one (0°) layup. The subscript s in the notation indicates the symmetry of the layup about the mid-plane. For example, the above multidirectional laminate can also be named as: $[0/45_2/90]_s$. [4]

Chapter 2 – Literature Review

To improve the efficiency of the machining processes, i.e. reduce the costs and increase the surface quality, researchers began studying Fiber Reinforced Polymer (FRP) composites. The main driving force behind this was to understand the complex interaction between the anisotropic inhomogeneous material and the tool as well as to predict the cutting forces and post-machined surface morphology. Studies into FRPs can be divided in three realms; analytical, experimental and numerical, which will be reviewed in the following sections.

2.1 Analytical Studies

Analytical studies mainly approximate the principal and thrust cutting forces using the continuum mechanics and Merchant's minimum energy theory.

Everstine and Rogers [5] proposed a theoretical model for machining FRP composites that predicts the minimum cutting force required for machining parallel unidirectional fibers (0°) based on a continuum mechanics approach [6]. Their proposal was similar to Palmer and Oxley's [7] thick-zone model for cutting metals. They explained the formation of wrinkle ahead of tool tip owing to tensile loading from the chip separation. Plastic deformation is found by using suitable displacement boundary condition and constraint conditions. They proposed an estimate for the principle cutting force, F_C in terms of the tool geometry, material properties and the proposed deformation. The schematic diagram of their cutting model is shown in Figure 2. Here, the workpiece is fixed on planes $X_1 = 0,$ and $X_2 = -H$ and *h* is the depth of cut, Also, $\underset{\sim}{a}$ and $\underset{\sim}{n}$ are unit vectors in tangential and normal directions to the fiber, respectively.

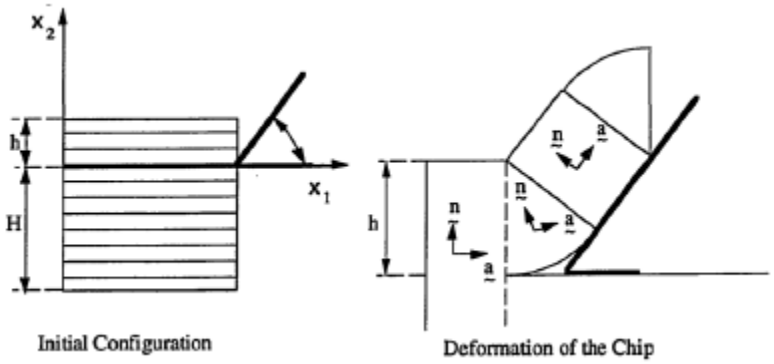

Figure 2 - Everstine and Rogers model for cutting composites [5]

Takeyama and Iijima [8] related their experimental observations to Merchant minimum energy theory to find the shear plane angle. Their model was restricted to FOs only between 0° to 60°, for which chip formation mechanism is virtually similar to that of metals. Schematic model used in this work is showed in Figure 3.

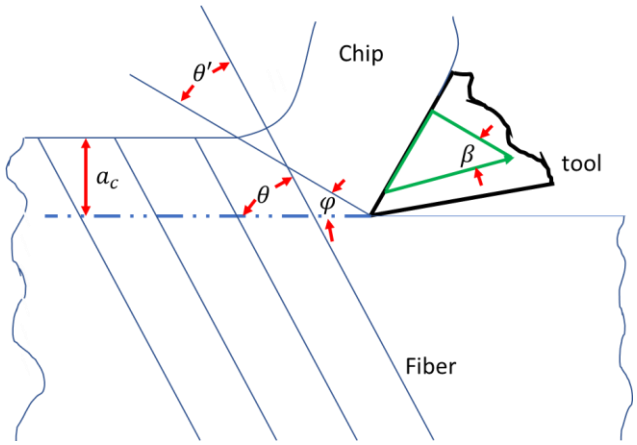

Figure 3 - Takeyama and Iijima orthogonal cutting model [8]

Where ϕ is the shear angle, θ is the fiber angle and θ' is the shear fiber angle, the angle between shear plane and fiber direction. Also, a_c is the depth of cut while α_0 and β are tool rake angle and friction angle, respectively.

In-plane shear angle can be obtained for different FOs by two methods: first, by running simple shear test experiments for different FOs and passing a curve through the experimental points. Equation 1 is the obtained equation for this curve which is obviously a function of shear fiber angle. [4]

$$\tau(\theta') = 23.03 + 0.10(\theta')^{1.63} + 0.26(\cos\theta')^{-7.71} \qquad \textbf{Equation 1}$$

The power during cutting process can be expressed in terms of in-plane shear strength, tool rake angle and the friction angle as in Equation 2. As only the cutting force, F_C , does the work for removing material, the power will simply be obtained by multiplying the cutting force by cutting velocity *V*. It should be noted that thrust force, F_t, is perpendicular to the cutting direction and does no work.

$$P = F_C V = \frac{V\tau(\theta')a_c a_w}{\sin\varphi}\frac{\cos(\beta-\alpha_0)}{\cos(\varphi+\beta-\alpha_0)} \qquad \textbf{Equation 2}$$

Here a_w is the uncut chip width. Takeyama and Iijima assumed shearing occur on a plane where the cutting energy is minimal. This means the derivative of Equation 2 with respect to fiber shear angle must be zero. Thus,

$$\frac{\partial\tau(\theta')}{\partial(\varphi)}\sin\varphi\cos(\varphi-\beta-\alpha_0) - \tau(\theta')\cos(2\varphi-\beta-\alpha_0) = 0 \qquad \textbf{Equation 3}$$

From Equation 1 and Equation 3, one can find the relationship between the shear giber angle and fiber orientation angle. Figure 4 shows the experimental and theoretical values of the cutting forces for the rake angle of 5°. Their model shows fairly good agreement

with experimental data for FO range between 0° to 60°. Unfortunately, this model was not sufficient to predict cutting forces for FOs above 75°.

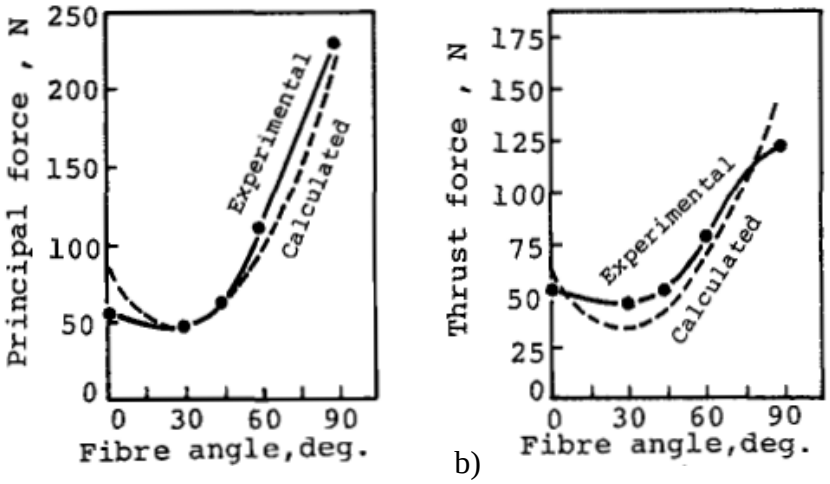

Figure 4 - experimental and calculated forces in Takeyama et al model; a) principle and b) thrust [8]

Bhatnagar et al [9] proposed a similar force prediction model to that of Takeyama and Iijima, assuming the shear plane angle lies in the FO angle ($\varphi = \theta$). They were able to capture experimental results closely only within the limited FO range of 10° to 60°. The in-plane shear strength of the CFRP material was determined by dividing the experimental shear force by the area of uncut chip size. Figure 5 illustrates the calculated and experimental in-plane shear strength results in Bhatnagar's [9] work.

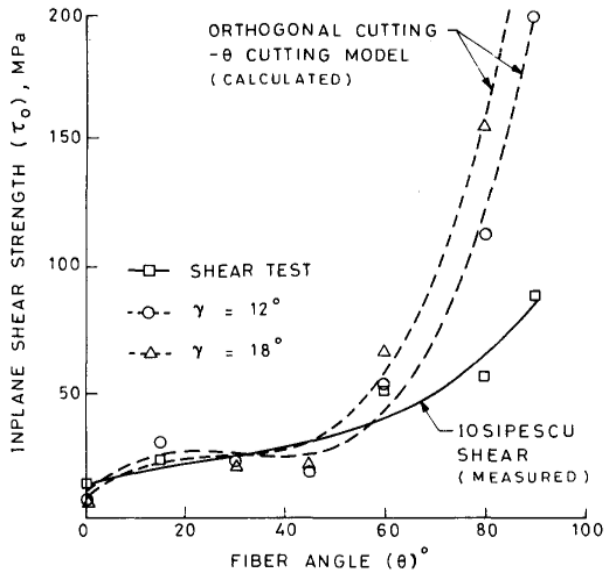

Figure 5 - comparison of in-plane shear strength between experimental and predicted [9]

Pwu and Hocheng [10] used the beam theory and laminate mechanics to study chip formation in cutting fibers perpendicular to cutting direction (90°). They concluded bending stresses are the main cause of fiber breakage.

Zhang et al. [11] introduced three regions when cutting FOs smaller than 90° based on experimental observations. These regions are shown in Figure 6 and are region 1: chipping, region 2: pressing and region 3: bouncing. Their work enlightened new understanding into chip formation mechanisms during FRP cutting.

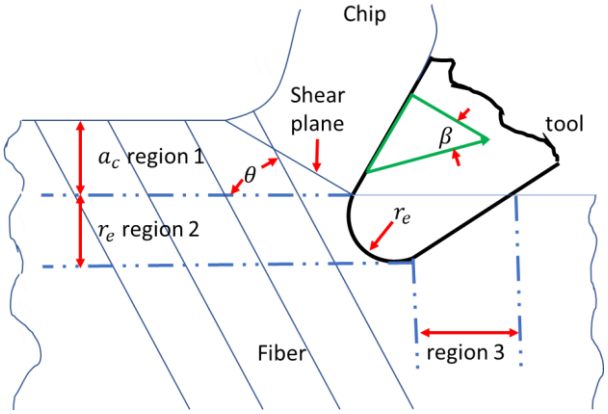

Figure 6 - Deformation regions for FO smaller than 90 [11]

The actual depth of cut is the chipping region depth (a_c). In the pressing zone, the material escapes cutting and undergoes elastic deformation as it is pushed under the tool nose. The thickness of this material is equal to the nose radius (r_e). In the bouncing region, material bounces back by elastic recovery. The thickness of this region is also assumed to be equal to the nose radius. The total cutting forces are obtained by the sum of the individual forces per each region. Figure 7 shows the predicted forces are in good agreement with experimental values but mainly for FO angles between 0° to 60°. The outstanding characteristic of this model is incorporation of tool geometry in predicting the cutting forces.

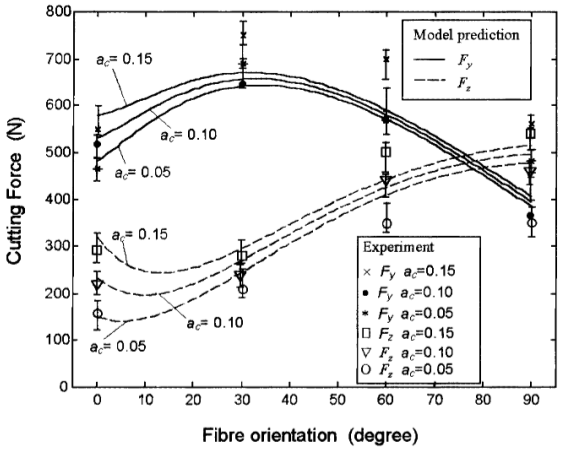

Figure 7 - Comparison between experimental and predicted forces [11]

2.2 Experimental Studies

As seen above, analytical models are accurate in predicting cutting forces only for a limited range of FOs. The reason for this is that the chip formation in this range is similar to metal machining. The shearing of the material is governed by its in-plane shear strength and the chip is formed by shearing along the FO. Furthermore, analytical studies lack information in regards to tool wear, chip formation and surface morphology after machining. Experimental studies, on the other hand, can provide excellent understanding of the above, especially with the help of high-speed camera and macrochip studies.

In 1983, Koplev et al. [12], studied chip formation mechanisms for the first time by running cutting experiments on UD CFRP specimens for fibers parallel (0°) and perpendicular (90°) to the cutting direction. They utilized “quick stop” and macrochip methods to investigate chip dimensions, surface morphology and cutting forces. They realized surface quality is affected by the FO and is better for cutting 90° FO compared to 0°. Koplev et al. also noticed that chips are created as the result of multiple brittle fractures rather than experiencing large plastic deformations. Figure 8 illustrates chip formation during cutting 0° and 90° fibers presented in their work. Tool geometry was considered in their work, concluding that increasing the rake angle would decrease the principal cutting force with negligible effect on the thrust force. On the other hand, increase in relief angle virtually did not change the principal cutting forces while slightly decreasing the thrust force.

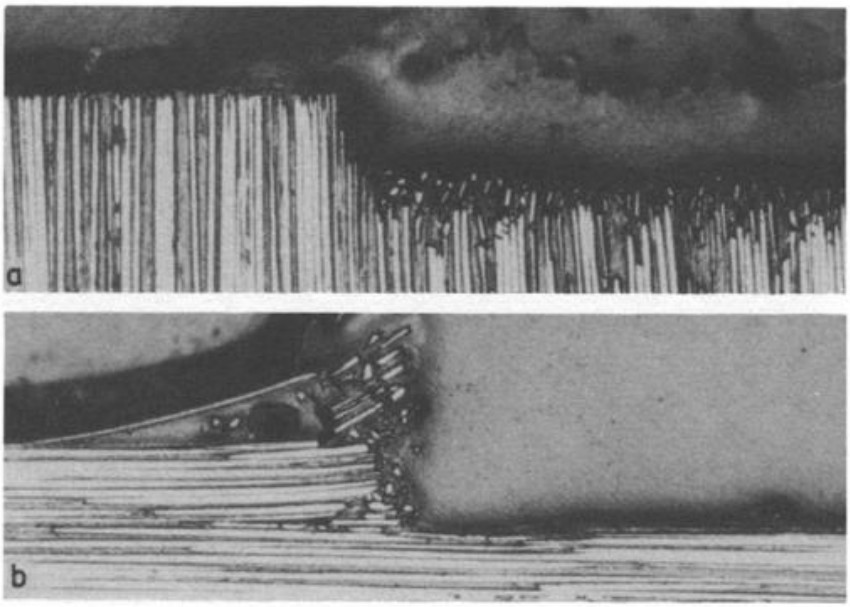

Figure 8 - chip formation presentation using 'quick-stop' method [12]

The same year, Sakuma and Seto [13] experimented with face turning of cylindrical GFRP pipes manufactured by filament winding process. To investigate the effect of FO, the GFRP pipes were wound right- and left-hand. Schematic diagram of the specimens used in their study is shown in Figure 9. They related the lesser amount of resistance in cutting left-hand material (positive FOs) to the difference in fracture mechanics of the

fibers, i.e. shear vs tensile strength, arguing that shear strength is relatively small to the tensile strength of the material. Surface roughness after turning of left-hand material reported to be similar to that of steel. However, high surface roughness observed for right-hand material. The reason behind this again was argued to be the fiber fracture mechanisms. They argued that in right-hand turning, the material is dug up by the tool leaving subsurface damages while the left-hand material fails because of the continuous frictional forces. Surprisingly, they attributed higher tool wear in cutting right-hand material to accumulation of heat and fiber ploughing.

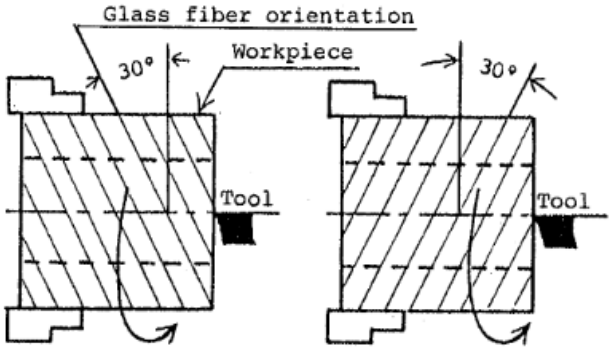

Figure 9 - illustration of GFRP specimens a) right-hand-wound b) left-hand-wound [13]

Hocheng and Pwu [14] reported three different types of chips: powder-like (45° fibers), ribbon-like (90° fibers - mainly by fiber breakage) and brush-like (for 0° fibers - unbroken segments still attached to the matrix showing interlaminar shear fracture). Fiber burrs were reported to occur at almost all FOs except for 0° due to interlaminar shear and fiber microbuckling fracture. These are caused by tool wear fibers and tool slip for 90° and lack of presence of pure shear for 45° fibers. To achieve a better surface quality, they recommended lower feed rates and higher cutting speeds.

In 1995, Wang, et al [15] observed three chip formation mechanisms with high-speed photography and macro-chip technique; For 0°, similar to what Hocheng and Pwu [14] concluded, fracture first occurs along fiber/matrix interface and then bending stresses cause second fracture perpendicular to the fiber axis. For FOs between 0° and 70°, compression-induced shear perpendicular to fiber axis is the dominant cause in chip formation. For FOs higher than 90°, both in and out-of-plane shear fracture along fiber/matrix interface occurs, creating macro fractures in composite material. They investigated surface morphology for FOs only up to 60 and reported that the average surface roughness in both longitudinal and transverse directions is almost the same for FOs 15°-60°. They also investigated tool geometry (clearance and rake angles) and concluded that low clearance angles increase the thrust forces while having almost no effect on principal forces. Higher rake angles when cutting 0° fibers reckoned as the result of chip formation mechanism change from microbuckling to peeling. Obviously, lower shear strength requires less force. For FOs between 15°-75° higher rake angles corresponded to higher forces, yet, having almost no influence on fiber angles 75-90.

Wang and Zhang [16], in 2003, reported FO as the most critical factor in the quality of the machined surface, 90° being the critical angle. They concluded higher FOs experience severe subsurface damage and bounce back due to elastic recovery of fibers under tensile bending loading is a characteristic of FRP machining. Three distinct deformation zones, i.e. chipping, pressing and bouncing introduced to cutting fibers under 90°. Depth of cut determines the type of deformation. For depths of cuts comparable to tool nose radius, while cutting fiber angles less than 90, compressive axial force is applied to the fibers. This will leave protruded fibers after the cut. When the depth of cut is higher than tool nose radius, perpendicular shear force causes fiber to fractures. Figure 10 shows the effect of depth of cut on the force at which force is applied. Fiber-matrix debonding results in deeper subsurface damage.

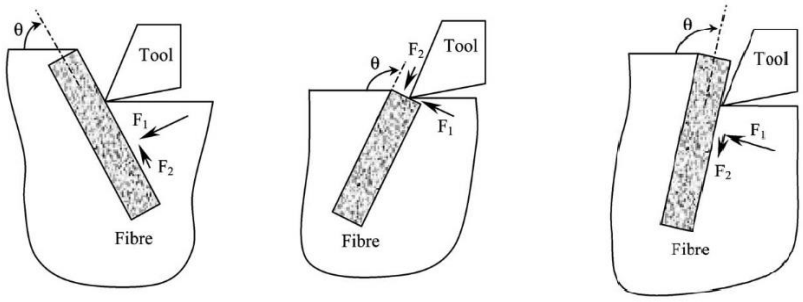

Figure 10 - deformation mechanisms based on depth of cut [16]

Rake angle was reported to have little effect on the surface roughness in the range studied. Curing conditions considered showed changes in mechanical properties of the specimens and consequently slight influence on the cutting forces.

Nayak et al [17] studied machining of UD-GFRP composites and published their work in two parts; experimental and finite element analysis. Given the lack in the literature by then, they investigated tool rake angle influence on negative fiber angles between 0° and -90°[1]. Chips were collected using double adhesive tape. A fluorescent dye was used to penetrate the specimen via cavities and cracks (Figure 11). When the specimen was exposed to ultraviolet light source, the damage zone could be seen. They reported that the cut fiber and chip size decrease generally when increasing negative FO from -15° to -90°. Figure 12 shows the reported variation of subsurface damage with respect to FO for two different depths of cuts.

[1] Negative convention is used for FOs between 90°-180°, for example -45° equals to 135°.

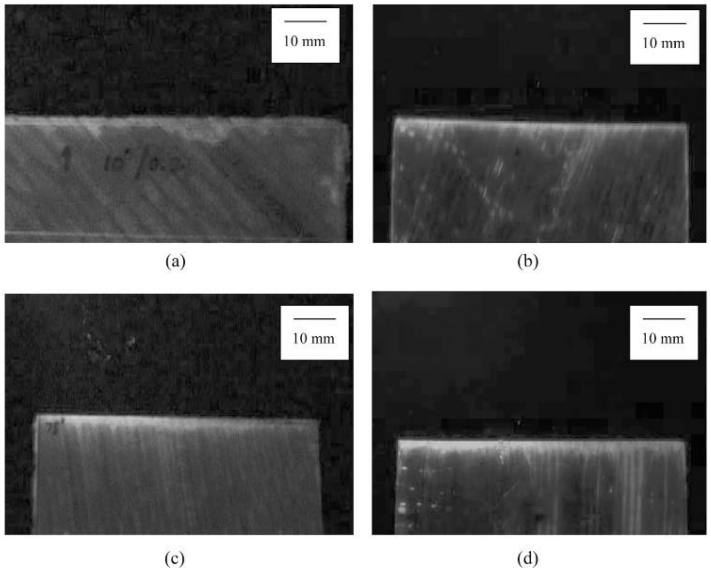

Figure 11 - Fluorescent dye technique for highlighting subsurface damage a) -45° b) -60° c) -75° and d) -90° [17]

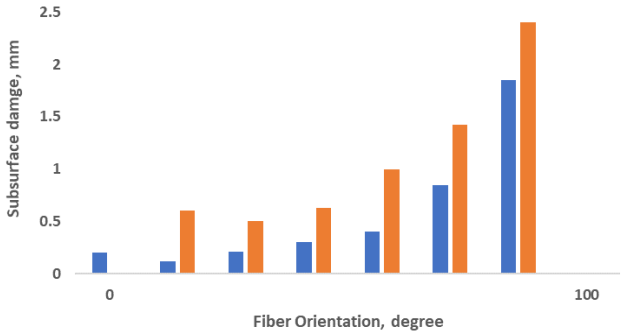

Figure 12 - variation of subsurface damage for two depths of cuts [17]

2.2.1 Mechanistic force prediction models

Mechanistic approach can be used in parallel to experimental studies to define force prediction models. These models do not have the limitations of the theoretical models. In mechanistic models, the cutting forces are directly predicted by using the specific cutting energy coefficients and chip geometry. Equation 4 shows the relationship between the cutting forces and specific cutting energy coefficients in tangential and normal to cutting directions.

$$F_C = K_C(a_c, \theta).a_c a_w$$
$$F_t = K_t(a_c, \theta).a_c a_w \qquad \textbf{Equation 4}$$

Where,

F_C and F_t are the principal cutting and thrust forces, respectively.

K_C and K_t are specific cutting energy coefficients in the principal cutting and thrust directions, respectively.

a_C and a_w are the depth and width of uncut chip, respectively.

θ is the fiber orientation.

Although mechanistic models are capable of capturing the forces in a wider range of FOs, they still rely on the experimental data, specifically the specific cutting energy[1]. For fiber reinforced materials, the specific cutting energy is dependent on the FO. [4] Principle and thrust cutting forces can be measured by using a dynamometer during the machining. Coefficients of specific energy can then be found by dividing the cutting forces by the chip geometry. The specific cutting energy changes with FO, gradually increasing with increase in FO from 0° to 75°. It then gets to the highest value at FO of 90°. After that a sharp decrease occurs and continues. Equation 5 [4] approximates the specific cutting energy for principal and thrust forces for GFRP by fitting a curve passing through the experimental data. [17]

$$K_C = a_C^{-0.4533}(61.3011 - 1.1926\theta + 0.0646\theta^2 - 0.0005\theta^3) \quad \textbf{Equation 5}$$
$$K_t = a_C^{-0.8375}(35.0636 - 0.095\theta^2 - 0.0001\theta^3)$$

[1] the amount of energy required to remove unit volume of material

2.3 Numerical studies

Experimental studies expanded researchers' insight over chip formation mechanisms during machining and its clear dependency on FO. With the help of high-speed cameras, four different mechanisms were observed. Table 1 summarizes the chip formation mechanisms based on FO.

Table 1 - Chip formation mechanism for different fiber orientations

FO (°)	Chip formation mechanism
0	• **Interface failure**; fiber matrix debonding, long strands of fiber yarns intact and detached from the matrix. • **Micro-buckling**; in case of high rake angles and/or and depths of cuts close to tool nose radius.
0-90	• **Shear-induced compressive** failure along fiber transverse axis, • Though interface fracture is not dominant, fiber burrs may appear due to large tool nose radii and small depths of cuts. • Often in cutting FO between 0-75, fibers resistant to compressive axial force, might not fracture and fiber bounce back happen.
90-135	• **Powdery chip**, short fibers are caused by fiber tension rupture. Fibers fail after bending-induced stresses exceed tensile strength of the material. • In- and out-of-plane macro-fracture.

Tool geometry (rake angle, clearance angle and tool nose radius), cutting conditions (depth of cut, cutting speed, spindle speed, feed rate) and work piece material (FO and curing conditions) all influence the results of an experimental study. Post-experimental procedures are also required to obtain target results, which can sometimes be time-consuming. The powdery chip produced during machining may jeopardize the health of the operator. It is also electrically conductive. Thus, if penetrated into the control system of the machine tool, it might cause short circuit problems. Experimental studies are then only good for understanding chip formation mechanisms, surface morphology and subsurface damage after cutting different FOs. Numerical studies, on the other hand, provide a good control over the large number of contributing parameters. Virtual machining simulations can eliminate the expensive cumbersome experiments.

Researchers have developed three approaches for numerical modeling for cutting FRP materials. These approaches are based on the scale on which the numerical solution is based. In Macro scale approach, an Equivalent Homogeneous Material (EHM) with orthotropic mechanical properties represents the UD laminate. The most appealing feature of this type of modeling is the time-effectiveness. Micro-mechanical models are more consistent with experimental results but consume a lot of time and energy. In this approach, matrix and fiber are modeled as individual phases. It is also vital to define the interaction mechanism between the two phases. The third approach, meso, is a combination of both macro and micro approaches to benefit from advantages of both. In a meso finite element model, the region adjacent to the tool is simulated in the micro scale

while the region far away from the tool is modeled as macro (EHM) to save the computational cost.

2.3.2 Macro modeling

In 1997, Arola and Ramulu [18] revealed the unrestricted capabilities of finite element models. The predicted orthogonal cutting forces in their 2D model had good agreement with their experiments. Thrust forces, however, were not in compliance with experiment results. Running a great deal of experiments, they defined two fracture mechanisms for a single chip formation. Primary fracture plane which lies on the trimming plane. Using In-situ optical techniques and post-process chip analysis they revealed that secondary fracture plane always occurs in the plane corresponding to fiber reinforcement direction for orientations between 15° to 90°. According to their experiments, orientation of the primary and secondary fracture planes when cutting fiber orientations larger than 90 was totally different. The primary fracture plane started at the tool point and continued either along or below the trim plane through fiber/matrix interface. Secondary fracture plane then starts from the end of primary fracture plane following an undetermined path to the free edge of the workpiece. To model the primary fracture, they used a critical stress criterion for compressive and shear stresses in fiber transverse direction. Figure 13 illustrates failure envelops (stress contours) for different FOs in Arola et al. [18] work. For primary fracture in the trimming plane, for fiber orientation of 0°, interlaminar tensile and shear strength were used as the critical stress components.

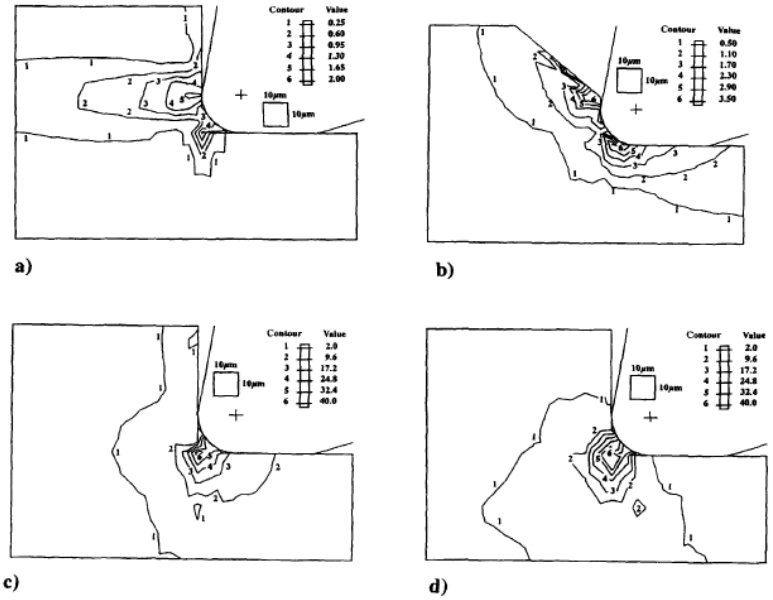

Figure 13 - Failure envelops near the tool a) 0° b) 45° c) 90° and d) 145° [18]

In 2002, Arola, Sultan and Ramulu [19] tried to study discontinuous chip formation through finite element modeling using the findings on their previous work [18]. In their updated model, principal cutting force prediction was improved. However, this was not the case for thrust forces. The authors attributed this to elastic recovery of the fibers and the consequent effect on the clearance angle. They reported maximum subsurface damage

in trimming Gr/Ep composite occurs at FO 90°. They also concluded that the stresses on the polycrystalline diamond tool was ten times smaller than the ultimate strength of the tool material. They investigated tool design parameters in three conditions concluding: 15° rake angle minimizes cutting forces; 10° rake angle creates the least subsurface damage and 5° rake angle produces minimal stress on the tool.

Mofid and Zhang [20] developed a 2D cutting model in ADINA based on quasi-static plane deformation conditions using a homogeneous anisotropic elastic material and Tsai-hill failure criterion for chip separation. They used Chamis Theory [21] to obtain Equivalent Homogeneous Anisotropic Material properties. Chamis assumed the ply to be orthotropic. Therefore, leaving only five independent elastic constants required. In order to use Chamis equations, fiber volume ratio (K_f), five fiber properties (E_{f11}, E_{f22}, G_{f12}, G_{f23}, and ν_{f12}) and two matrix properties (E_m and ν_m) are needed. Mofid and Zhang, then defined the global stiffness matrix of the material using EHAM properties. Transformation matrices used whenever the material and geometrical axes do not coincide. Tsai-hill criteria applied to simulate chip separation. They found the biggest cutting forces when cutting FO of about 100°. One interesting point they claimed in their report for higher stress magnitudes in plane stress conditions is the fact that one stress component is zero. Hence, lower stresses are computed during simulation which requires higher stress levels for satisfying the criteria. In response, higher forces are needed to separate the chip. Figure 14 shows the discrepancy between simulated and experimental values caused plane stress assumption. They compared their results with experimental results obtained by Wang and Zhang [22] and claimed good agreement with experimental results and no significant effect for the rake angle. They attributed the discrepancies between experimental and simulated results to the process of homogenization of the material.

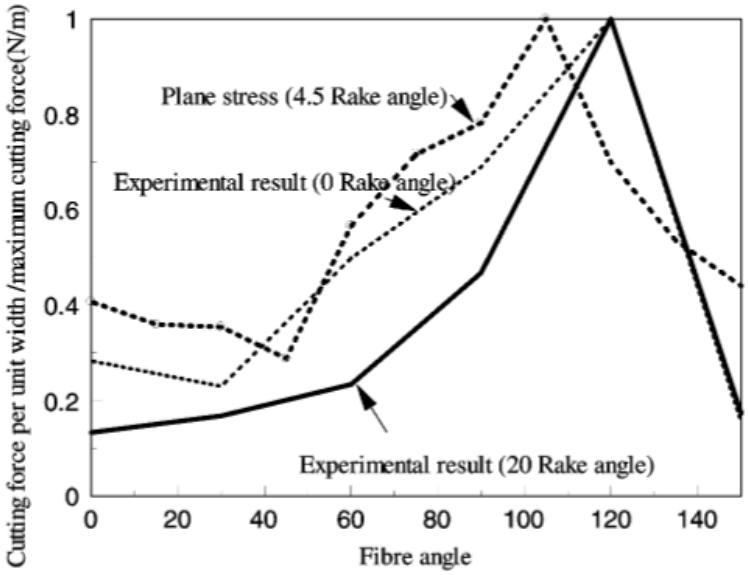

Figure 14 - Cutting forces versus fiber orientation for anisotropic EHM [20]

Santiuste et al [23] adopted a dynamic approach to macro-mechanically simulate initiation and completion of chip formation. The mechanical properties of Carbon fiber epoxy and GFRP composites were obtained from the study on these materials in an international exercise (World-Wide Failure Exercise) [24] [25]. Fiber orientations considered are 15°, 30°, 45°, 60°, 75°, and 90°. The EHM in their model was defined to behave elastically up to the point of failure. Damage initiation (onset of degradation at a material point) was based on Hashin criterion. They found that CFRP is considered to be brittle while GFRP is a ductile composite material. Energy required to complete the chip formation was accounted for the degree of ductility. They found better surface quality after machining for CFRP compared to GFRP. This was also attributed to the higher energy absorption during large deformation of glass fibers and subsequent surface damage below tool tip. Figure 15 shows the numerical results compared to experimental and numerical data presented in [26] and [27], respectively.

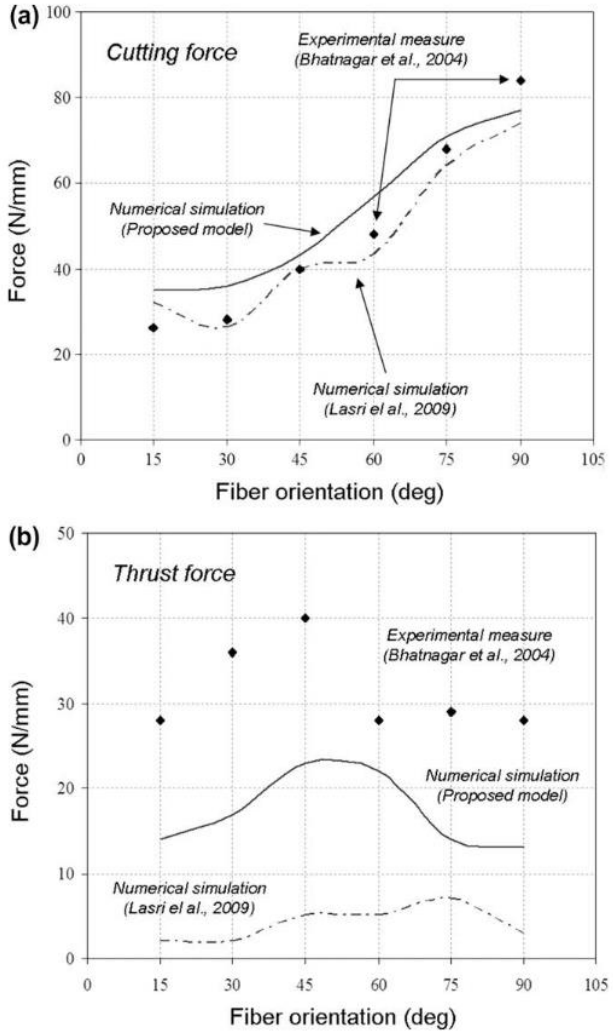

Figure 15 - comparison of a) principal and b) thrust forces in Santuise macro-model to experimental data [26] and Lasri [27] numerical work [23]

Nayak et al [28] developed a macro and a two-phase micro model and compared their results with respect to fiber orientation, depth of cut and tool rake. They incorporated the effect of friction in the macro FE model. The coefficient of friction was determined using pin-on-disk experiments for several fiber orientations. They reported that FRP components encounter more frictional resistance when machined at higher fiber orientations.

Since the experimental observations revealed the chips are discontinuous and powdery in shape, the values for frictional coefficients are utilized in the FE model only for the flank surface of the tool and not the rake face. A full-scale model of the experimental specimen is used and the material is defined as anisotropic but locally homogeneous. Contact pairs were established between the chip surface and the machined surface along the trim plane to simulate debonding and chip formation. Contact pairs were also used between chip and tool surface as well as between the machined surface and tool to prevent the inter-penetration of surfaces into one another. Two different failure criteria, one for node debonding along the trim plane due to specified critical stress and other ahead of the deboned node due to Tsai-Hill for chip release is used. The cutting force and thrust force during the simulation are calculated from the reaction exerted by the work-material on the reference point of the rigid tool when debonding takes place. The extent of the spread of Tsai-Hill envelope below the trim plane is considered to be the sub-surface damage. The average deviation between the simulated and experimental values of cutting force is found to be between ±10% only. However, the trend for thrust forces does not match with experimental results and the average deviation is found to be ±38% as can be seen in Figure 16. It should be noted that their model could was limited to fiber orientations up to 90°.

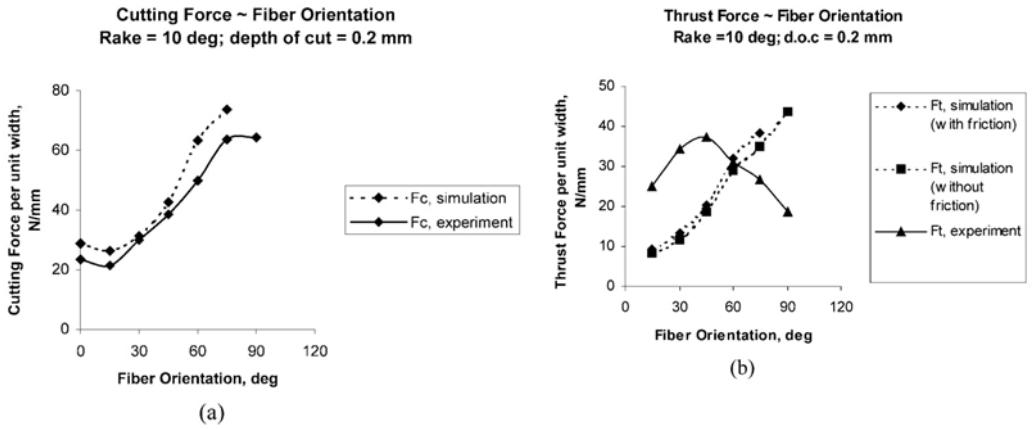

Figure 16 - comparison of Nayak macro-model force results with experimental data a) principal b) thrust [28]

The authors reported that both cutting and thrust forces decreased with increasing tool rake angle. Poor agreement for the thrust force results with experimental data was associated to material constituent model (EHM) and ignorance of subsurface damage during cutting. Higher degree of subsurface damage will effectively reduce the magnitude of thrust force for higher fiber orientations.

2.3.3 Micro and Meso modeling

In order to investigate the discrepancies in the thrust force prediction, Nayak et al. [28] developed the two-phase FE model consisting of both fiber and matrix properties for orthogonal cutting. To save the computational costs, they used a single fiber [28]. The bottom edge of the model fixed and the left edge is constrained to move in vertical direction only. The tool assumed to be a rigid body. Fiber and matrix both assumed to be isotropic. Duplicate nodes are placed in all the elements situated along the fiber-matrix interface. Node release happens when the normal and shear strength of fiber-matrix interface is overcome due to the tool movement. The node separation at the fiber-matrix interface is continued until the fiber fracture initiates. The side of the fiber facing the tool is found to be subjected to a localized principal compressive stress near the point of contact whereas the area just outside the tool-fiber contact zone is under principal tensile stress. Authors claim that for all the fiber orientations, the fiber tensile strength is achieved earlier as compared to the compressive strength. Cutting and thrust forces show better trend agreement to experimental data (Figure 17). The magnitude is obviously not comparable due to the fact that simulation is conducted with a representative monofilament. As can be seen in Figure 17, this model also is limited to FOs up to 90°. Simulated subsurface damage followed experimental results only up to FO of 60° for just lower depths of cuts. As the depth of cut increased, actual subsurface damage remains higher than simulated one.

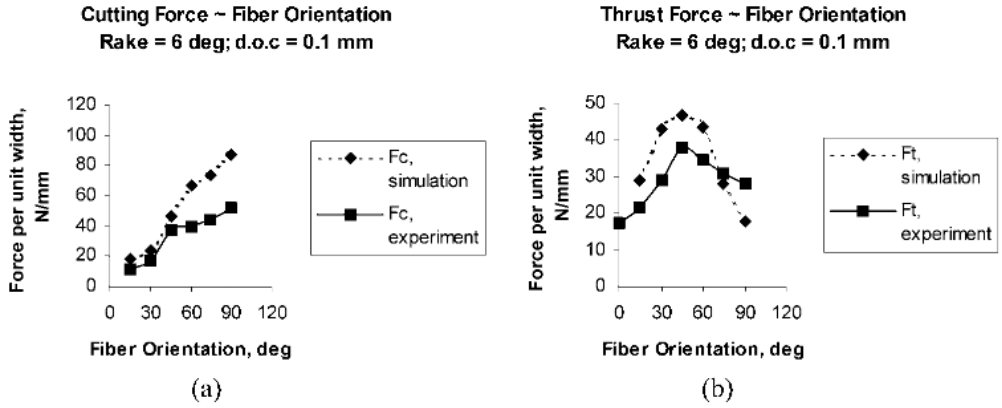

Figure 17 - comparison of Nayak micro-model force results with experimental data a) principal b) thrust [28]

Rao et al [29] developed a micro mechanical finite element model in 2007 for plane strain quasi-static orthogonal cutting of CFRP and GFRP assuming fiber to be elastic and matrix to be elaso-plastic. Their results were better when compared to Nayak's work [28]. This was mainly because they added matrix damage (elastic modulus degrading), matrix isotropic hardening and debonding zone for fiber/matrix interface (cohesive zone model – CZM) to the model. In their model, fiber failure occurs when maximum principal stress exceeds tensile strength. Matrix failure occurs when ultimate strength is reached. They assumed the tool as a rigid body because the elastic modulus of carbide tool is 2.5 and 6 times of that of fiber and matrix, respectively. Material properties used in their study is summarized in Table 2.

Table 2 - material properties used in Rao's et al. micro model [29]

Material	Property	
Fiber (carbon)	Elastic constants (tension)	$E_{11}=235GPa, E_{22}=14GPa, G_{12}=28GPa, \nu_{12}=0.2$
	Elastic constants (compression)	$E_{11}=110GPa, E_{22}=14GPa, G_{12}=28GPa, \nu_{12}=0.2$
	Tensile strength	$X_t=3.59GPa, Y_t=0.35GPa$
	Compressive strength	$X_c=1.8GPa, Y_c=2.73GPa$
	Shear strength	$S=0.38GPa$
	Diameter	$d=10\mu m$
Fiber (glass)	Elastic constants	$E=72GPa, \nu_{12}=0.22$
	Tensile strength	$\sigma_t=3.4GPa$
	Diameter	$d=10\mu m$
Matrix (epoxy)	Elastic constants	$E=3.1GPa, \nu_{12}=0.33$
	Tensile strength	$\sigma_t=70GPa$
Fiber-matrix interface	Normal strength	$160MPa(UD-GFRP), 167.5MPa(UD-CFRP)$
	Shear strength	$34MPa(UD-GFRP), 25MPa(UD-CFRP)$
	Work of separation	$50N/m(UD-GFRP), 50N/m(UD-CFRP)$
EHM (UD-CFRP)	Elastic constants	$E_{11}=140GPa, E_{22}=11GPa, G_{12}=6GPa, \nu_{12}=0.38$
EHM (UD-GFRP)	Elastic constants	$E_{11}=35.9GPa, E_{22}=4.55GPa, G_{12}=3.83GPa, \nu_{12}=0.38$

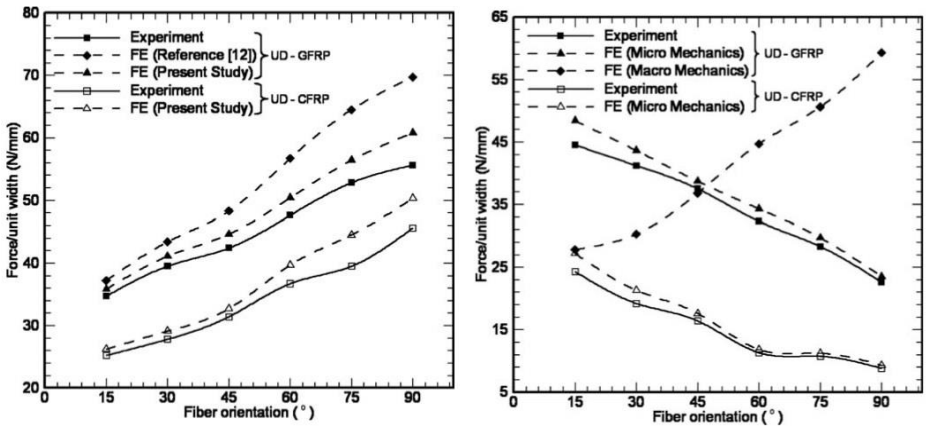

Figure 18 - validation of simulated a) principal, b) thrust forces with experimental data [29]

Figure 18 shows fairly well agreement between the predicted cutting forces and experimental reported data. Yet, the results reported were again only for FOs between 15° to 90°.

Dandekar et al [30] incorporated Marigo model [31] to simulate brittle fracture of carbon fibers. Simulated stress results of CFRP machining is shown in Figure 19. Effect of imperfections in carbon fiber on its failure was included in this model. Carbon fibers usually have randomly distributed defects on their surfaces or in the interior. The presence of these defects results in fluctuations in the experimentally determined strength data. The damage evolution assumed to depend on the Weibull distribution of the strength of the carbon fibers. In other words, they considered statistical variations in fiber strength.

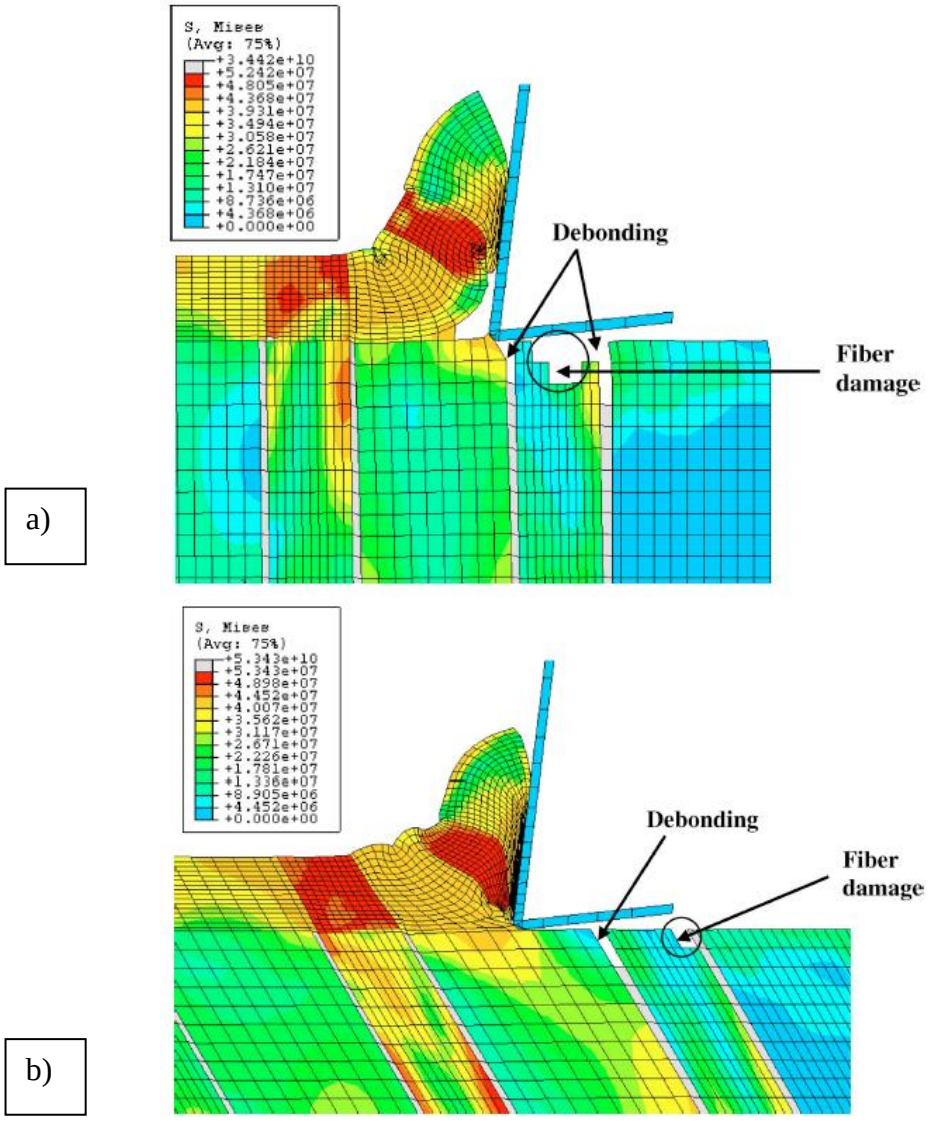

Figure 19 - Dandekar simulated stress results for cutting a) 90° b) 45° CFRP [30]

Mkaddem et al [32] developed a micro-macro (meso) model for orthogonal cutting of GFRP. They reported satisfactory prediction for cutting forces. They used Tsai-hill criterion to simulate cutting of the Equivalent Orthotropic Homogeneous Material (EOHM). The authors compared the force results with those of [17] and [28] as can be seen in Figure 20. Their model showed better agreement with experimental data

compared to the work of Nayak for principal cutting forces. In the case of thrust force, the model was able to capture the experimental trend (increase up to the 45-fiber angle and then decrease up to 90). The model, however, is limited to FOs up to 90°. They also concluded that increase in rake angle will result to a decrease in both cutting and thrust forces.

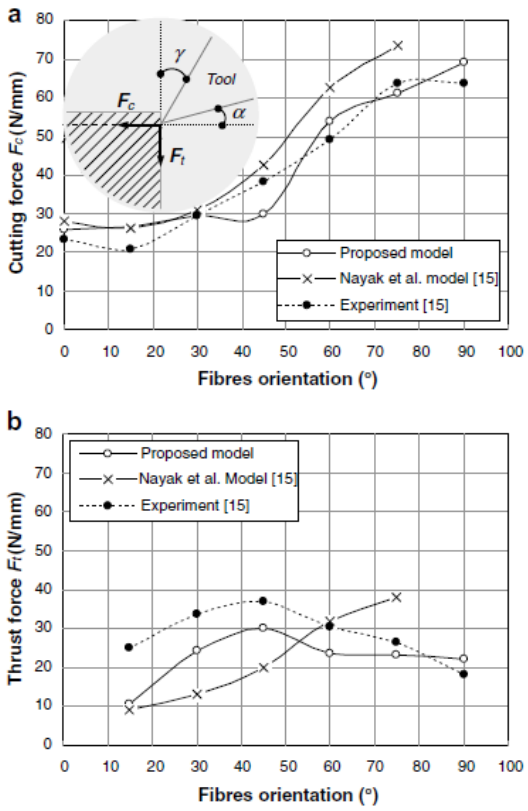

Figure 20 – Mkaddem simulated and experimental results for a) principal and b) thrust forces [32]

Calzada et al. [3] developed a micromechanical finite element model incorporating velocity-based boundary (dynamic[1]) condition for tool movement instead of displacement for FOs 0°, 45°, 90° and 135°. They used continuum cohesive elements to model the interface. Cohesive zone modeling of the interface involves challenges in dynamic modeling. Cohesive elements can bear only tensile stresses. Any longitudinal or transverse compressive loading will cause excessive distortion in elements and simulation abort. Since Calzada et al [3] used continuum approach for the cohesive elements, they had to define a small (near zero) thickness for these elements. Very small thickness of the cohesive zone imposes significant decrease in the lowest stable time increment of the simulation. [33]. This will increase the computational time drastically. The authors used normal and tangential damage progress models for the interface continuum elements. In their model, damage evolution (reduction in elastic modulus of the interface) was defined exponentially. They used three parameters to characterize the microstructure of the

[1] Refer to Appendix 1 for more info on dynamic/static analysis

material; a) fiber angle, b) fiber grouping number and c) matrix spacing. Several microstructures were analyzed using Scanning Electron Microscopy (SEM) technique. Figure 21 shows the simulated specimen versus the real one. Obtained force results are compared with average experimental data in Figure 22.

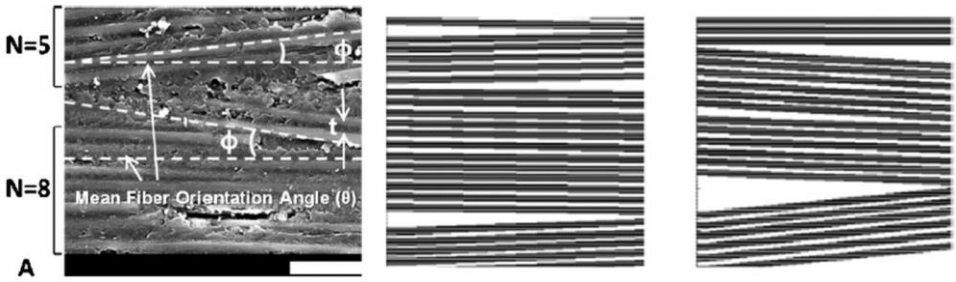

Figure 21 - real specimen and simulated microstructure in Calzada's work [3]

It should be noted that the thrust forces magnitude is significantly smaller compared to experimental data. Authors attributed this to the absence of elements after failure and incapability of holding stress. They also reported that factors other than FO such as tool geometry and fiber diameter can change the fiber failure mode. For instance, decreasing the fiber diameter from 7.5 µm to 3.5 µm, increasing the tool rake angle from 25° to 50° and decreasing the tool edge radius from 5 µm to 1 µm changed the fiber failure mode from bending to crushing for FO of 135°.

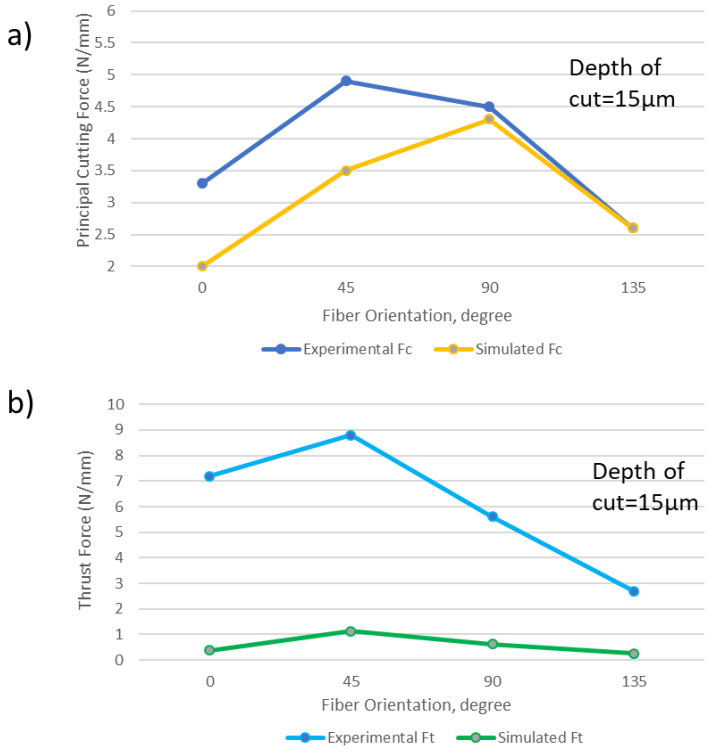

Figure 22 - comparison of simulated a) principal b) thrust cutting forces with average experimental force data in Calzada's work [3]

Abena et al [2] developed a 2D finite element model in 2015 while focusing on a novel approach to simulate cohesive zone between fiber and matrix. The problem of the cohesive zone elements in the literature reported to be the lack of capability to withstand compressive forces. They added a small thickness (2.5 µm) to the element to accommodate the compressive stresses. Fibers deemed to fail when the maximum principal stress criterion is satisfied. Matrix behaviour was simulated as an elaso-plastic material. Failure in matrix occurs when Von Mises stress reaches the ultimate strength of material. Three FOs of 45, 90 and 135 were investigated and predicted principal and thrust force results compared to the experimental data from Calzada's work [3]. This model reported to capture principal forces for 90° and 135° very well (within 5%). However, the thrust force results were again underestimated by far. Figure 23 shows the comparison between simulated and experimental results.

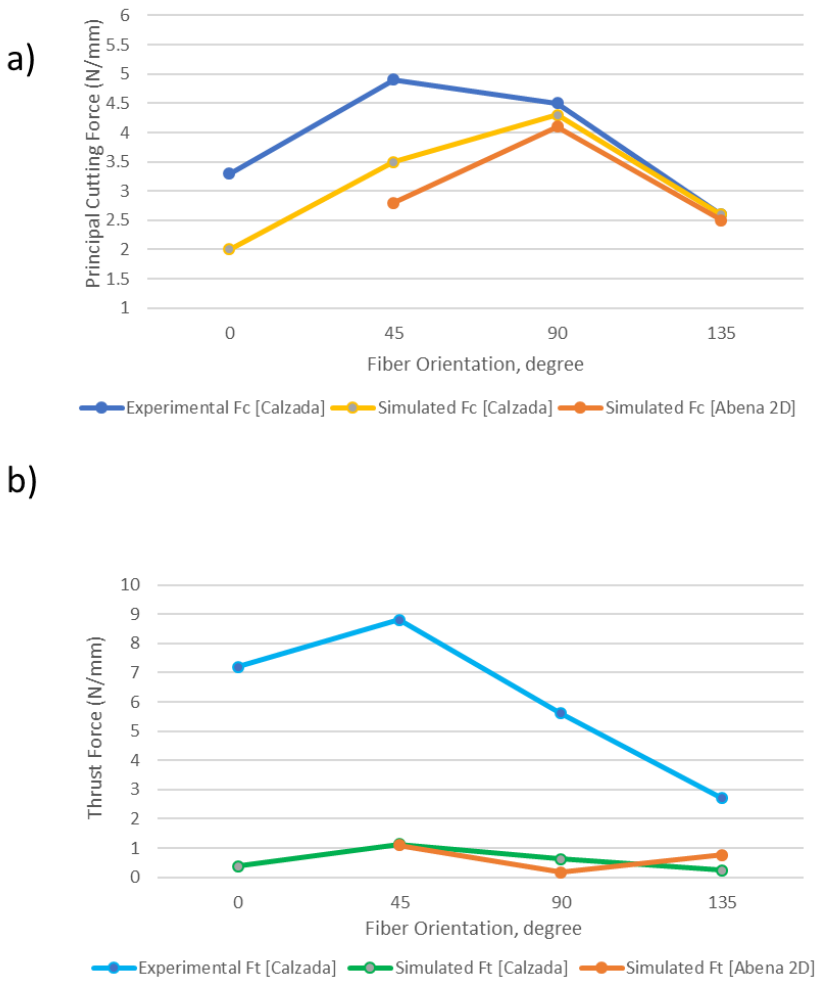

Figure 23 - Comparison between simulated and experimental force results in Abena's 2D model [2]

Two years later, in 2017, Abena et al [1] introduced a 3D model by simply using mean extrusion of their previous work [2]. Material behavior defined the same as their previous work. However, the thickness for interface was now eliminated via using the unique

method of surface cohesive behavior simulation in ABAQUS. In their model, zero thickness cohesive elements fail if the surrounding material, fiber or matrix, fail. Material properties used in their model is summarized in Table 3. It should be noted here that the values in this table are the ones used in the present thesis for comparison purposes.

Table 3 - Material properties of the FE model [3] [2] [1] [34] [35]

Material	Property	Value
Carbon fiber	Elastic constants	E_1=235 GPa, E_2=E_3=14 GPa ν_{12}= ν_{13}=0.2, ν_{23}=0.25 G_{12}=G_{13}=28 GPa, G_{23}=5.5 GPa
	Longitudinal Strength	X_t=3.59 GPa, X_c=3.0 GPa
Epoxy	Elastic constants Yield strength	E=2.96 GPa, ν=0.4 σ_y=74.7 MPa
Interface	Normal Strength Shear Strength Fracture Energy	σ_{max}=167.5 MPa τ_{max}=25 MPa G_c=0.05 N/mm2
EHM	Elastic constants	E_1=142.18 GPa, E_2=E_3=7.606 GPa ν_{12}= ν_{13}=0.28, ν_{23}=0.347 G_{12}=G_{13}=4.151 GPa, G_{23}=2.824 GPa

Predicted cutting and thrust forces were validated to experimental results are shown in Figure 24. Good agreement is reported for predicted principal forces for FOs 90° and 135°. It should be noted that fibers are modeled in rectangular shape and are not fully embedded in matrix material.

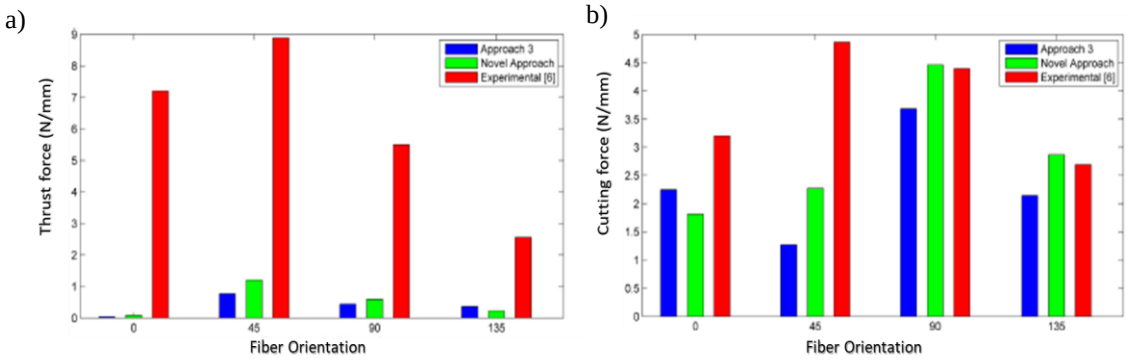

Figure 24 - comparison between simulated and experimental forces for a) Abena et al. 2D [2] and b) Abena et al. 3D work [1]

Chapter 3 – Numerical Model

In the present work, ABAQUS/Explicit platform is used to build a dynamic three-dimensional finite element model for simulating the cutting process of CFRP unidirectional material. To simulate fairly high cutting velocity realistically, a dynamic explicit analysis is selected. The finite element model is in 'meso' scale; consisting of a micro-scale model adjacent to the tool tip and a macro-scale equivalent homogeneous material further away from the tool to provide adequate stiffness during the cut. Material properties, tool geometry, tool-workpiece interaction, boundary conditions and other simulation assumptions are explained in this chapter.

3.1 ABAQUS/Implicit (Standard) VS ABAQUS/Explicit (dynamic)

ABAQUS implicit analysis is usually used for static analyses. Newton-Raphson iterative method [36] is utilized in ABAQUS implicit to solve a system of equilibrium equations [37] based on force and displacement boundary conditions

$$[F]-[K][U]=0 \qquad \textbf{Equation 6}$$

It should be noted that for this method to be convergent, accurate initial approximation is crucial. Algorithmic restriction exists in ABAQUS to limit the increment size. The bigger the increment, the more time would be required for higher number of iterations.

ABAQUS explicit analysis, on the other hand, uses dynamic response at the end of each increment as the initial conditions for the next increment. Accordingly, global stiffness matrix is not created. Thus, there is no need to solve the system of equilibrium equations for the elements simultaneously. ABAQUS uses Equation 7 to solve an explicit analysis. [37]

$$[P]-[I]=M\ddot{U} \qquad \textbf{Equation 7}$$

Where P , I , M and $\ddot{U}$ are the external load, internal load, lumped mass and displacement matrices, respectively. ABAQUS explicit uses Euler forward (central difference) method [36] for integration. Table 4 summarizes the differences between Implicit and Explicit analyses in ABAQUS.

Table 4 - differences between Standard and Explicit analyses in ABAQUS

Implicit	Explicit
Displacement, velocity and acceleration equations are solved simultaneously with Newton-Raphson iterative method.	Displacement, velocity and acceleration equations are solved at each time increment using data from previous increment. No iteration occurs at time increment to solve the system of equilibrium equations.
Displacement and forces are computed using local and global stiffness matrices.	No stiffness matrix is produced during simulation.
Trial and error procedure occur in	ABAQUS uses internal criteria such as

approximating the roots of the equation using Newton's method. If the initial approximation is too far from the actual root value or the increment size is too big the solution will not converge.	excessive distortion and kinematic energy to abort the simulation.

3.2 Material definition

As mentioned before, meso scale is used in this numerical study. Near the tool tip, three separate phases are modeled, i.e. Carbon fiber, Epoxy matrix and the interface bonding between them. An Equivalent Homogeneous Material (EHM) is included further away from the tool to provide necessary stiffness in tool movement direction and save computational cost. Material properties used in the present model are the same as the ones used in references [1]–[3] for the sake of comparison. These properties are summarized in Table 3.

3.2.1 Matrix

Matrix material used in this model is a thermosetting polymer (epoxy). Thermoplastics are also used as matrix. Elastoplastic behavior has been defined for this phase of the CFRP composite. Elastic behavior of the material is defined by the Young modulus and Poisson ratio. Matrix yields when the equivalent Von Mises stress exceeds the yield strength of epoxy and elements fail when ultimate strength is reached. Isotropic hardening (cold work) has been included in material definition. The softening response (plastic behavior) of the matrix is characterized by stress-displacement relation rather than stress-strain relation. The reason behind this is because after damage occurs, stress-strain response can no longer predict material behavior. Damage in the matrix is characterized by two factors: degradation of the material elasticity and softening of the yield stress. Ductile damage mechanism built-in ABAQUS is used to simulate progressive damage of matrix material. This type of damage is the consequence of nucleation, growth and coalescence of voids. A damage initiation criterion is required to define the initiation point of each damage mechanism. Then, the damage will progress (damage evolution) based on a defined damage evolution criterion until the elements are deleted. Damage variable, D, at damage initiation point is zero. As the equivalent plastic strain increases, the value of D increases to maximum value of 1. [33] Ductile damage used for the matrix is explained in Appendix 1.

3.2.2 Fiber

Carbon fibers are modeled cylindrical with diameter of 7.5 µm [1]–[3]. Unlike an isotropic material, in which elastic properties are the same in all directions, mechanical properties along the axis of the fibers are much stronger than transverse direction in a CFRP unidirectional laminate. Carbon fibers are modeled to behave as transversely isotropic materials. To do so, a VUMAT subroutine is written which reads the inputs per increment from ABAQUS and gives the computed outputs back to the software. The subroutine is written for orthotropic materials. Obviously, one can define transversely isotropic material by choosing identical Poisson's ratios, Young and Shear moduli for two transverse directions perpendicular to fiber axis. For more information on transversely isotropic materials please refer to Appendix 4. Fibers are defined to behave

purely elastic with no plastic deformation as supported by experiments.[12], [23], [30] Maximum principle stress criterion is used to simulate brittle fiber failure. [1]–[3] Fiber elements fail when maximum tensile/compressive principal stresses exceed the tensile/compressive strengths of the material. [38]

3.2.3 Interface

The cohesive behavior of the bonding phase between fiber and matrix can be modeled using two basic methods in ABAQUS:

1. Element-based approach
2. Surface-based approach

In the element-based method, the interface behavior can be defined by two different sets of laws: continuum or traction-separation. In the former, material properties and behavior of the cohesive elements are defined in the property module of the software. The cohesive elements can be embedded into an existing 3D mesh or modeled as a separate part. The shortcoming of the first approach is the inability of the elements to withstand compressive stresses. In the latter, zero-thickness cohesive behavior can be modeled even for more complicated surface shapes. This is a better representative of real situation were carbon fibers are usually impregnated in epoxy matrix and cured to final shape obtained.

In the present model, the second approach, surface-based cohesive, is used. Master and slave surfaces are selected as the fiber and matrix surfaces. General contact is used for all other contact interactions such as tool fiber surface. Cohesive behaviour is simulated by defining interaction properties in the 'Interaction' module of ABAQUS [33] and contact enforcement algorithms used for the interactive surfaces. Three stiffness coefficients are defined for three different planes (normal, shear 1 and shear 2). These are constant mechanical properties of the bonding phase. Using numerical equations and contact algorithms the software finds the initiation point of the damage. Uncoupled mode is used for the three damage variables in the present study. This means the effect of stiffness degradation in the normal direction is not affected by the effects of stiffness degradation in the other two orthogonal directions. Properties of the interface are defined as in Table 3 to be consistent in result comparison with literature. Figure 25 shows the principle behind traction-separation law in ABAQUS [33]. Indices *n*, *m* and *s* refer to normal only, tear and shear modes, respectively. t_n^0 is the displacement at the onset of damage in normal direction. Same definition is applied to *m* and *s* directions. Damage evolution can be defined either by defining displacement at failure or a relation for fracture energy in the three orthogonal planes.

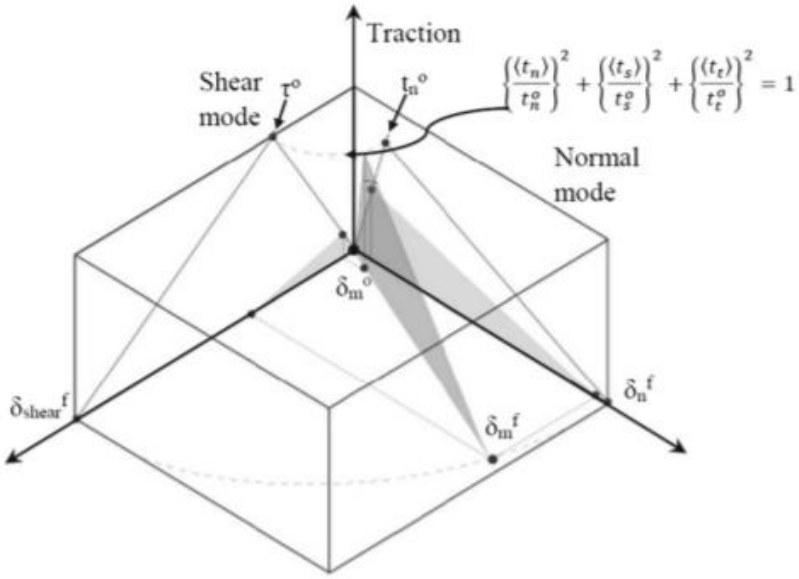

Figure 25 - traction-separation law for simulating the interface bond behavior between fiber and matrix [33]

3.2.4 Tool

Since modulus of elasticity of the tool is much higher than that of the fiber or matrix, it is modeled as a rigid body. The analytical surface of the tool is defined for contact purposes. A reference point is assigned and tasked to capture the cutting forces during each simulation step. Tool rake and clearance angles are 25° and 10°. Tool nose radius is 2 microns. Figure 26 represents tool geometry used in the present work.

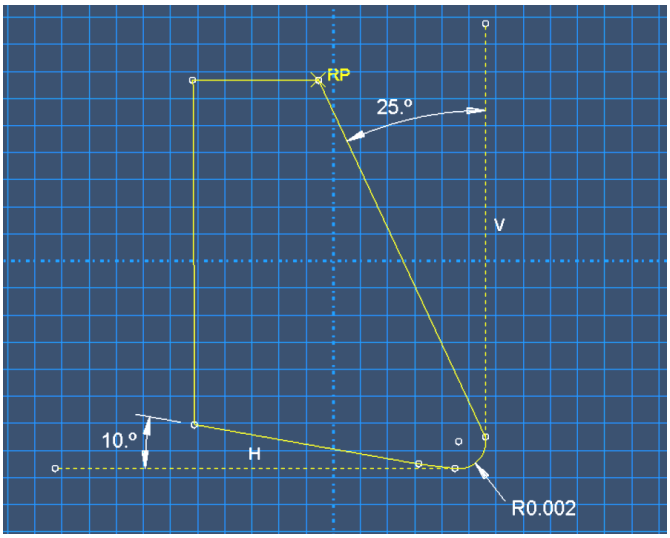

Figure 26 – Tool geometry used in the present work

3.3 Mass scaling

Mass scaling is used to increase the minimum stable time increment. Mass adjustment for elements is proportional to the "pre-adjusted"[1] mass of those elements. Hence, the center of mass and the principal directions of the rotary inertia do not change. For more information on time stability and mass scaling refer to Appendix 1.

3.4 Contact enforcement algorithm

Penalty contact enforcement algorithm built-in ABAQUS is used in the present model, as this is the default contact algorithm defined for general contacts in ABAQUS. Cohesive zone is modeled by defining cohesive contact properties and assigning those to master and slave surfaces. For more details on contact algorithms in ABAQUS refer to Appendix 1.

3.5 Boundary conditions

The translational and rotational displacement for bottom face of the 3D CFRP workpiece is restrained in all directions. The left face is allowed to move only in Y direction. Velocity-based boundary condition of 0.5 m/min is applied to the reference point of the rigid body tool.

3.6 Nonlinearity

Three following sources of nonlinearity can be found during a numerical simulation.

i. **Material behavior**, plastic behavior and damage propagation mechanisms in epoxy matrix are two examples of material nonlinearity included in the present work.

ii. **Boundary conditions,** boundary conditions might change during the simulation as illustrated in Figure 27. Contact conditions during the simulation can be considered as nonlinearity in this model.

iii. **Geometrical effects,** to better understand this type, assume a column under buckling loading. At the beginning of the loading, force P is applied right at the center of the column. As deflections increase, the insertion point of the force recedes from the original axial direction of the column leading to change of loading conditions (Figure 28) due to newly-introduced moment of force P at the fixed support. This kind of nonlinearity in included in the present developed model.

Figure 27 – example of nonlinearity in boundary condition

[1] Preadjusted mass is the element attributed mass due to material density definition in property module.

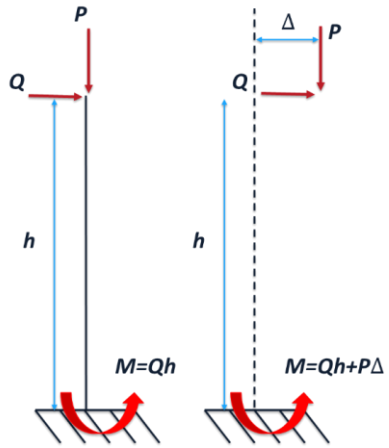

Figure 28 – example of geometrical nonlinearity

3.7 Formulation

Mathematical theory to define the element behavior is called formulation. Two descriptions of behavior can be defined: Lagrangian (material) and Eulerian (spatial). In the former, elements deform with the material while in the latter, elements are fixed in the space and material flows through them. Adaptive meshing combines features of both behaviors. This type of analysis is called Arbitrary Lagrangian-Eulerian (ALE) analysis. Adaptive mesh can often maintain a high-quality mesh under severe material deformation by allowing the mesh to move independently of the underlying material. Figure 29 shows a rigid die of sinusoidal shape deforming a blank of steel with and without using ALE. [33]

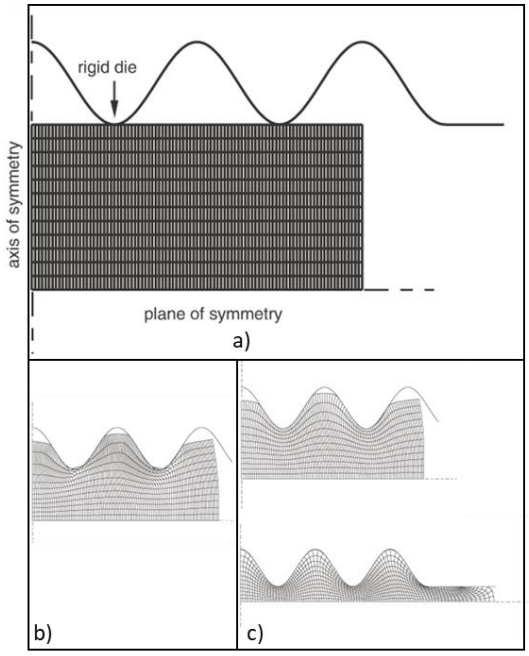

Figure 29 - forge forming simulation of a rectangular steel plate b) simulation terminated due to excessive distortion in elements c) simulation completed using ALE [33]

Chapter 4 – Results and Discussion

In this chapter results of the simulations are presented. In the first section, Von Mises stress contours are shown for different FOs for the sake of realization of chip formation mechanisms. Subsurface damage is defined as the depth of the failed cohesive elements between fiber and matrix to represent the fiber-matrix debonding phenomenon. This was measured by the help of a dimensionless contact damage state variable, CSDMG, predefined in ABAQUS and the color code spectrum in the final results. This damage variable varies between 0 and 1. Material points are active when CSDMG equals zero and failed when CSDMG equals one. Simulated principal and thrust cutting forces are shown afterwards. These are the average of the forces during the time step of the analysis. Representation of simulated data is then followed by a discussion and comparison with experimental and numerical results in literature. At the end of this chapter, room for improvement and future work is discussed.

4.1 Von Mises stress contour

Figure 30 to Figure 33 show the numerical results for Von Mises stress contours for fiber orientations 0°, 45°, 90° and 135°, respectively. These figures include three sets of images at three different time instants. The upper image shows the fibers embedded inside the matrix material while the bottom image illustrates fibers only at the same time instant.

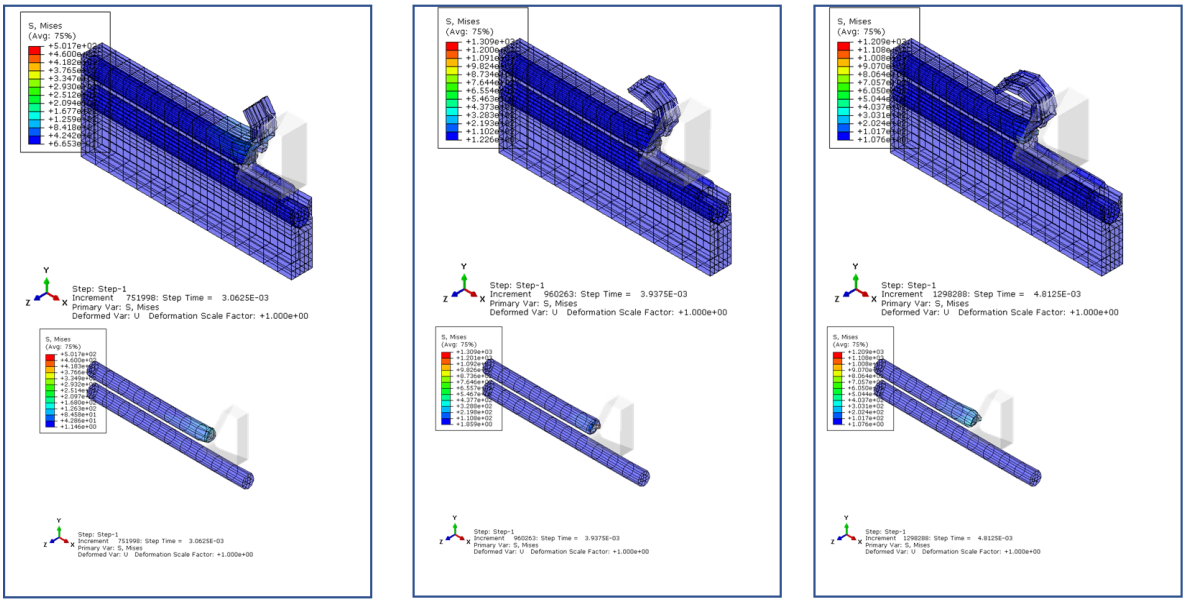

Figure 30 - Von Mises stress contour for 0° FO

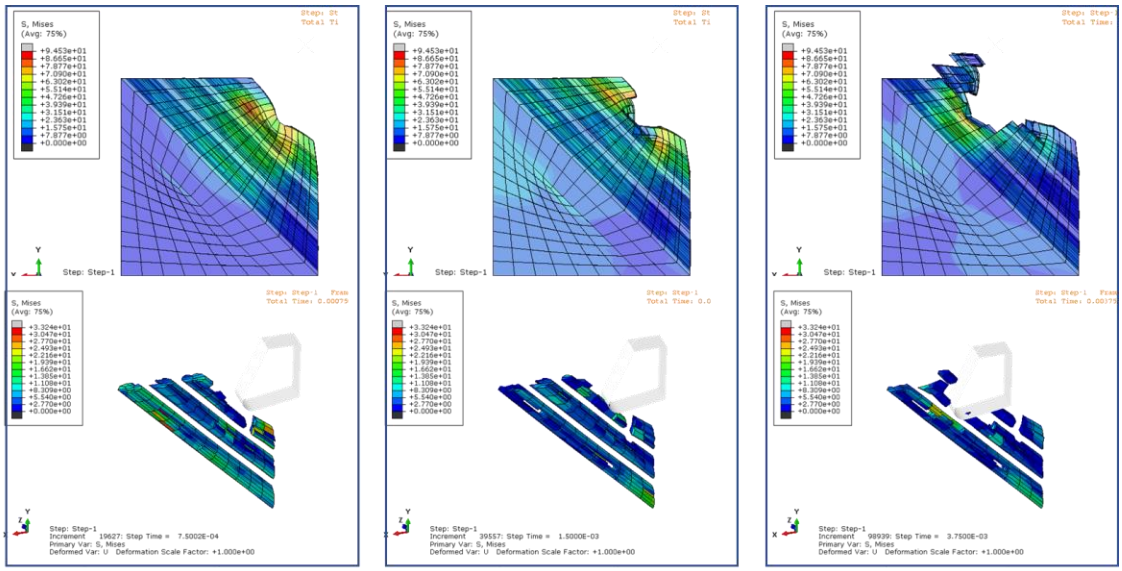

Figure 31 - Von Mises stress contour for 45° FO

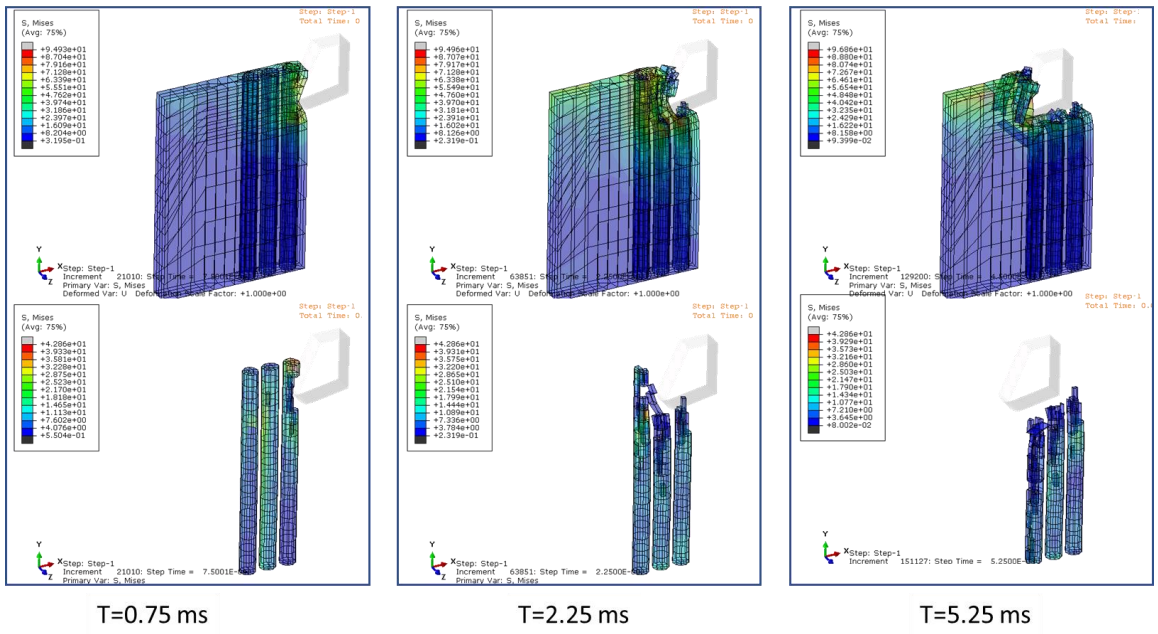

Figure 32 - Von Mises stress contour for 90° FO

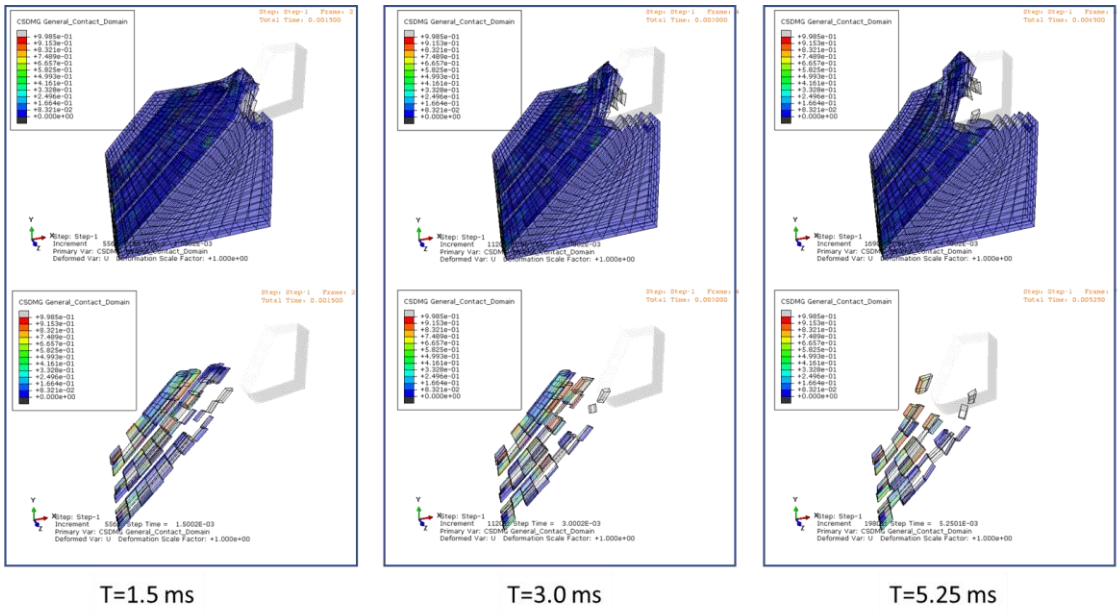

Figure 33 - Von Mises stress contour for 135° FO

4.2 Subsurface damage

Figure 34 to Figure 37 show the subsurface damage results for FOs 0°, 45°, 90° and 135°, respectively. It should be noted that CSDMG state variable in ABAQUS is used as a measure for the illustration of the subsurface damage in the model. This variable is dimensionless and varies between zero and one. Material points are deleted when the value of CSDMG reaches unity. For almost all fiber orientations, subsurface damage due to interface bonding failure is noticeable. Rainbow color code is used for distinguishing the failed material points from active ones.

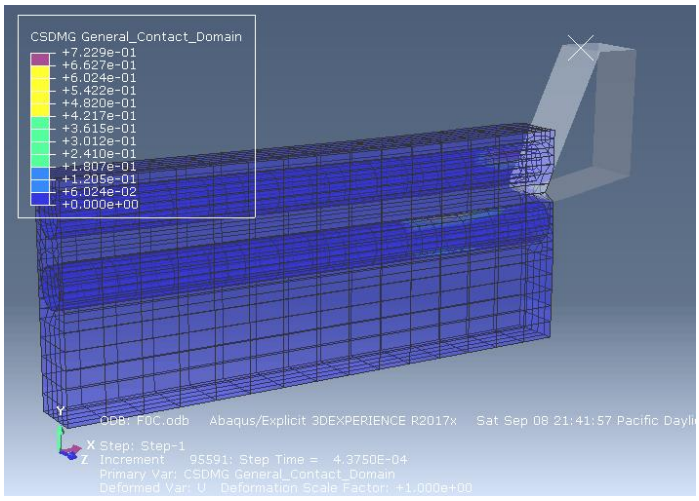

Figure 34 - simulated subsurface damage for 0° FO

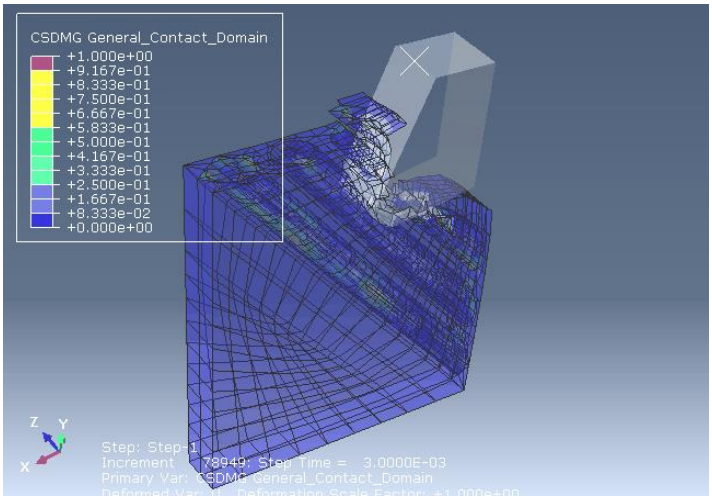

Figure 35 - simulated subsurface damage for 45° FO

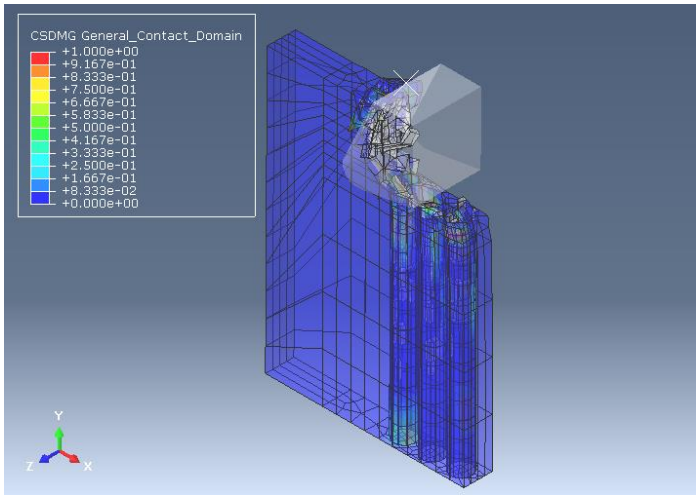

Figure 36 - simulated subsurface damage for 90° FO

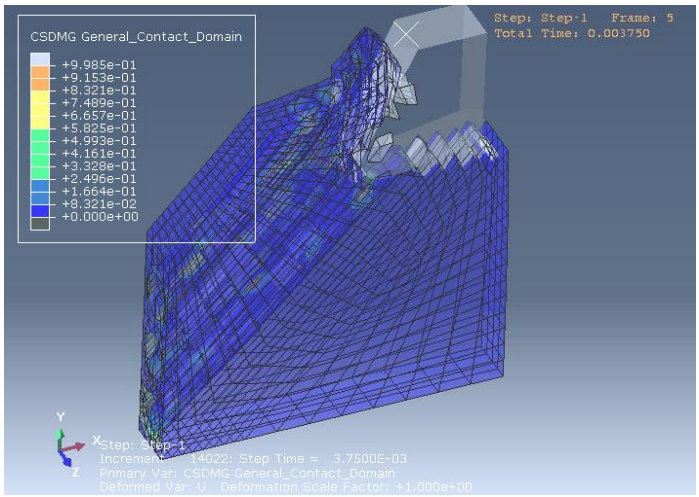

Figure 37 - simulated subsurface damage for 135° FO

4.3 Cutting forces

Figure 38 to Figure 41 show the principal cutting and thrust force results for fiber orientations 0°, 45°, 90° and 135°, respectively. Forces are averaged over the period of analysis time step to be able to compare with experimental and literature results.

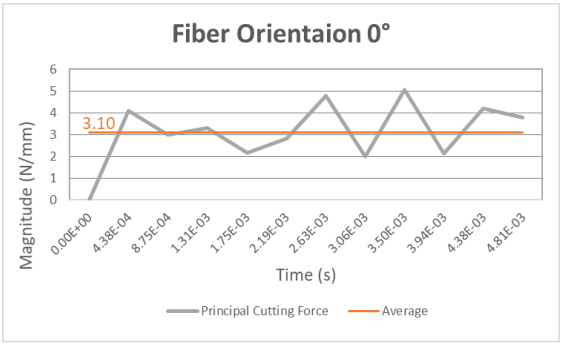

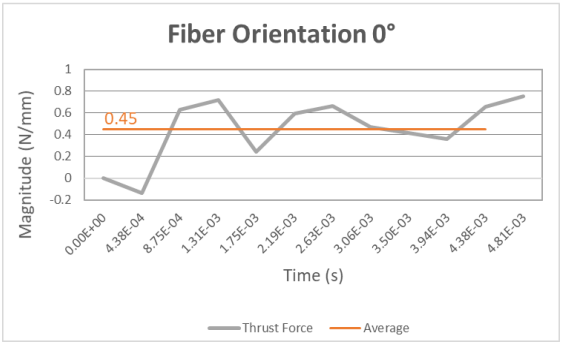

Figure 38 - predicted principal and cutting force results for FO 0°

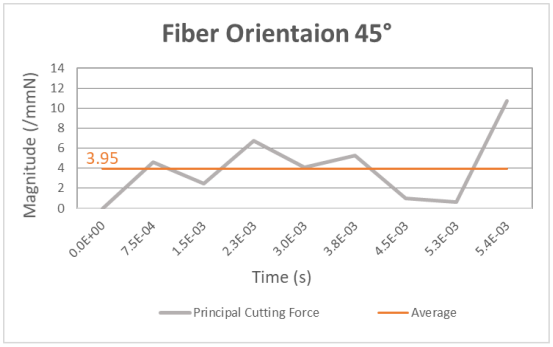

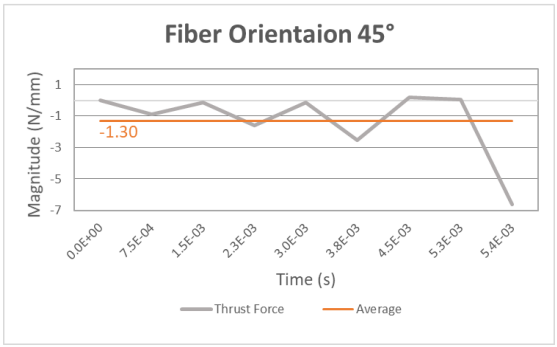

Figure 39 - predicted principal and cutting force results for FO 45°

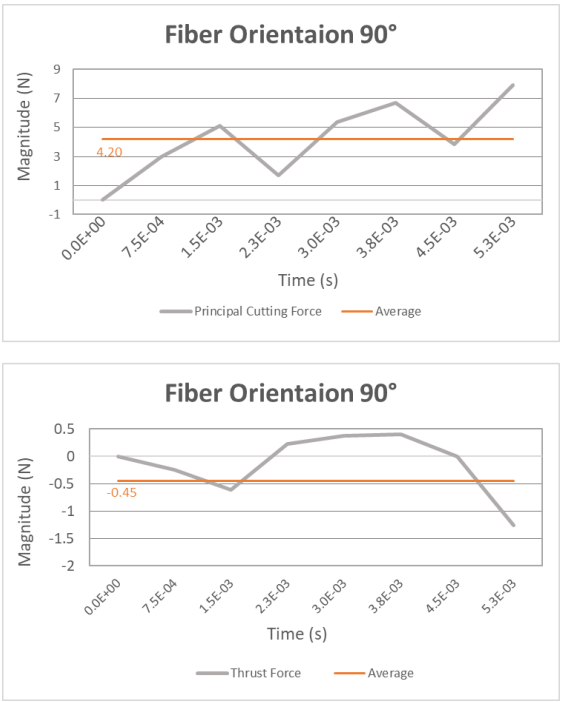

Figure 40 - predicted principal and cutting force results for FO 90°

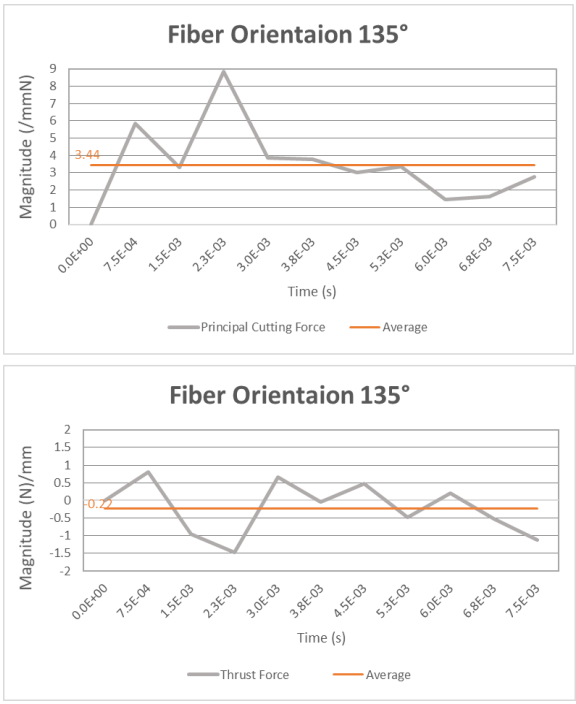

Figure 41 - predicted principal and cutting force results for FO 135°

4.4 Discussion

The numerical principal and thrust cutting forces are validated by the experimental data in Calzada et al. [3] work as well as numerical data in Abena et al 2D and 3D models [1], [2]. Figure 42 and Figure 43 summarize this comparison. Unlike Abena et al [1] 3D model where fibers were rectangular, fibers in the present work are modeled as cylindrical entities. This is a better representation of reality. Also, fibers in Abena 3D model are not embedded fully in material. In other words, left and right sides of the fibers are free faces while in the present work, fibers are totally embedded in matrix material. Also, two damage models, ductile and shear, are incorporated in the present model for better representation of the matrix material response. The simulated principal cutting force trend and magnitude is in good agreement with experimental results while the thrust forces are still underestimated.

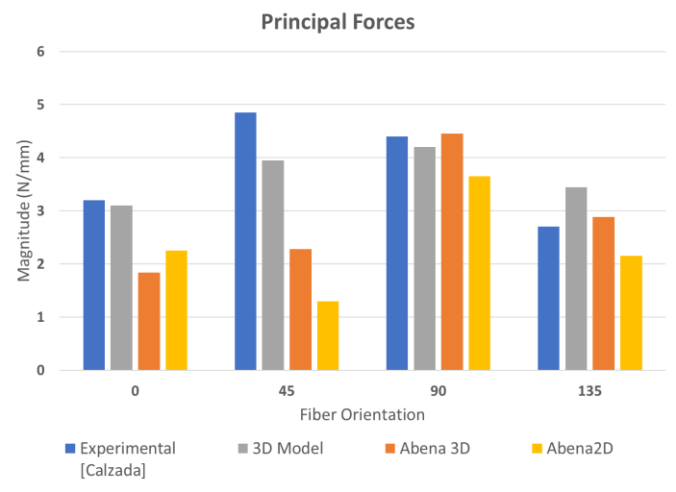

Figure 42 - comparison of simulated principal forces with experimental [3] and numerical data [1], [2] in literature

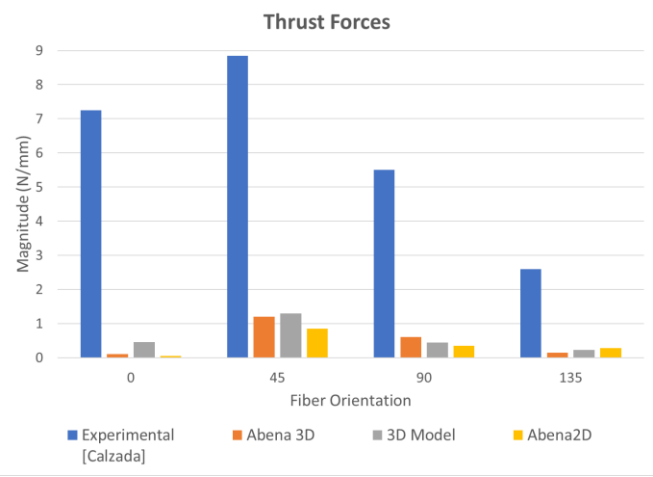

Figure 43 - comparison of simulated thrust forces with experimental [3] and numerical data [1], [2] in literature

Reported numerical cutting forces are the mean average over the analysis time. Principal cutting forces agree well with experimental data. The principal force increases with fiber orientation from 0° to 45°. This is due to the fact that chip formation mechanism changes from microbuckling to compressive-induced shear fracture in FO 45°. The principal force then continues to decrease up to the smallest magnitude in FO 135°. This is again attributed to the chip formation for FOs higher than 90°. Bending-induced shear is the predominant chip formation mechanism for these FOs. The average deviation from experimental results for principal cutting forces is about 13% while it is less than 5% for FOs 0° and 90°. Thrust force results, on the other hand, are still underestimated. Although the model is able to capture the trend of the force fluctuation with respect to FO, the predicted results are of approximately an order of magnitude smaller than the experimental data. This increases the uncertainty of the predicted thrust force results. The thrust force underestimation can be associated with the different chip formation regions as elaborated by Zhang et al. [11]. The elastic recovery of the fibers after the tool passes them, can apply thrust force on the clearance face of the tool. [1], [18] This might be due to the tool being blunt and lack of pure shear fracture. It should be noted that underestimation of the thrust forces in the finite element model can also be the result of elements being deleted from the cutting plane after they fail. Thus, the contact between tool and workpiece is lost and the elements can no longer withstand stresses. [2], [3]

Subsurface damage is defined in this work as the depth of failure in interface bonding below the trim plane. This variable is used to represent the fiber matrix debonding. Failure for the interface elements is determined by use of CSDMG state variable predefined in ABAQUS to collect the material points at which failure has occurred. CSDMG variable varies between zero to one for active and deleted material points, respectively. Rainbow color code is used in the result visualization spectrums to show the deleted elements. Color red represents the failed elements. For 0° fiber orientation, damage along the interface observed in the longitudinal direction and the extend of the damage below the trim plane has the least value amongst all other fiber orientations. Numerical results show an upward trend for fiber matrix debonding depth with increase in fiber orientation. Approximate depths of subsurface damage for all four FOs is shown in Figure 44.

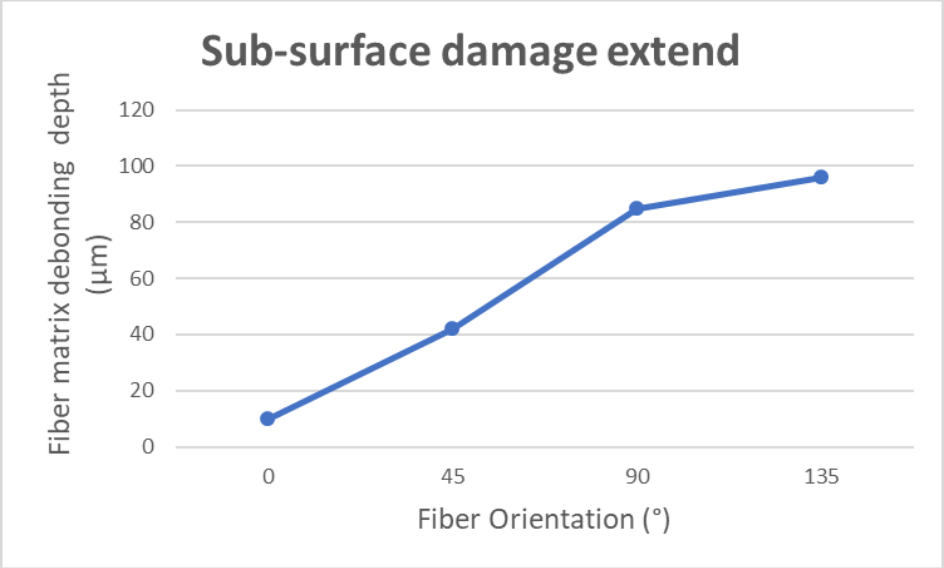

Figure 44 - subsurface damage with respect to FO

4.5 Future work

The thrust force cutting forces in the present work are underestimated. The main reasons behind this can be the bounce back (elastic recovery) of carbon fibers as well as deleton of load bearing element after full degradataion of the material. Thrust force reliance on tool geometry, especialy clearance angle, can be further investigated.

Subsurface damage is defined as the depth of fiber matrix debondign highlighted by CSDMG contact damage state variable. Unfortunately, due to lack of experimental and numerical data in literature, the predicted results could not be validated. Experimental work is required to obtain a basis for evaluation. Ultimately, this 3D cutting force prediction model can be extended to simulate milling or drilling processes and used for optimization of the tool path or geometry in order to achive better surface quality and less tool wear.

Finally, the model can be developed to be used for vibration-assisted machining by defining different angular acceleration or velocity-based boundary conditions for the tool at wisely selected time steps.

Bibliography

[1] A. Abena, S. L. Soo, and K. Essa, “Modelling the orthogonal cutting of UD-CFRP composites: Development of a novel cohesive zone model,” *Compos. Struct.*, vol. 168, pp. 65–83, 2017.

[2] A. Abena, S. L. Soo, and K. Essa, “A Finite Element Simulation for Orthogonal Cutting of UD-CFRP Incorporating a Novel Fibre-matrix Interface Model,” *Procedia CIRP*, vol. 31, pp. 539–544, 2015.

[3] K. A. Calzada, S. G. Kapoor, R. E. DeVor, J. Samuel, and A. K. Srivastava, “Modeling and interpretation of fiber orientation-based failure mechanisms in machining of carbon fiber-reinforced polymer composites,” *J. Manuf. Process.*, vol. 14, no. 2, pp. 141–149, 2012.

[4] J. Ahmad, *Machining of Polymer Composites*. Springer US, 2009.

[5] G. C. Everstine and T. G. Rogers, “A Theory of Machining of Fiber-Reinforced Materials,” *J. Compos. Mater.*, vol. 5, no. 1, pp. 94–106, Jan. 1971.

[6] J. F. Mulhern, T. G. Rogers, and A. J. M. Spencer, “A Continuum Model for Fibre-Reinforced Plastic Materials,” *Proc. R. Soc. Math. Phys. Eng. Sci.*, vol. 301, no. 1467, pp. 473–492, Nov. 1967.

[7] W. B. Palmer and P. L. B. Oxley, “Mechanics of Orthogonal Machining,” *Proc. Inst. Mech. Eng.*, vol. 173, no. 1, pp. 623–654, Jun. 1959.

[8] H. Takeyama and N. Iijima, “Machinability of Glassfiber Reinforced Plastics and Application of Ultrasonic Machining,” *CIRP Ann.*, vol. 37, no. 1, pp. 93–96, 1988.

[9] N. Bhatnagar, N. Ramakrishnan, N. K. Naik, and R. Komanduri, “On the machining of fiber reinforced plastic (FRP) composite laminates,” *Int. J. Mach. Tools Manuf.*, vol. 35, no. 5, pp. 701–716, May 1995.

[10] H. Y. Pwu and H. Hocheng, “Chip Formation Model of Cutting Fiber-Reinforced Plastics Perpendicular to Fiber Axis,” *J. Manuf. Sci. Eng.*, vol. 120, no. 1, p. 192, 1998.

[11] L. C. Zhang, H. J. Zhang, and X. M. Wang, “A FORCE PREDICTION MODEL FOR CUTTING UNIDIRECTIONAL FIBRE-REINFORCED PLASTICS,” *Mach. Sci. Technol.*, vol. 5, no. 3, pp. 293–305, Nov. 2001.

[12] A. Koplev, A. Lystrup, and T. Vorm, “The cutting process, chips, and cutting forces in machining CFRP,” *Composites*, vol. 14, no. 4, pp. 371–376, Oct. 1983.

[13] K. Sakuma and M. Seto, “Tool Wear in Cutting Glass-fiber-reinforced Plastics : The Relation between Fiber Orientation and Tool Wear,” *Bull. JSME*, vol. 26, no. 218, pp. 1420–1427, 1983.

[14] H. Hocheng, H. Y. Puw, and Y. Huang, “Preliminary study on milling of unidirectional carbon fibre-reinforced plastics,” *Compos. Manuf.*, vol. 4, no. 2, pp. 103–108, Jun. 1993.

[15] D. H. Wang, M. Ramulu, and D. Arola, “Orthogonal cutting mechanisms of graphite/epoxy composite. Part I: unidirectional laminate,” *Int. J. Mach. Tools Manuf.*, vol. 35, no. 12, pp. 1623–1638, Dec. 1995.

[16] X. M. Wang and L. C. Zhang, “An experimental investigation into the orthogonal cutting of unidirectional fibre reinforced plastics,” *Int. J. Mach. Tools Manuf.*, vol. 43, no. 10, pp. 1015–1022, Aug. 2003.

[17] D. Nayak, N. Bhatnagar, and P. Mahajan, “MACHINING STUDIES OF UNI-DIRECTIONAL GLASS FIBER REINFORCED PLASTIC (UD-GFRP) COMPOSITES PART 1: EFFECT OF GEOMETRICAL AND PROCESS PARAMETERS,” *Mach. Sci. Technol.*, vol. 9, no. 4, pp. 481–501, Dec. 2005.

[18] D. Arola and M. Ramulu, “Orthogonal cutting of fiber-reinforced composites: A finite element analysis,” *Int. J. Mech. Sci.*, vol. 39, no. 5, pp. 597–613, May 1997.

[19] D. Arola, M. B. Sultan, and M. Ramulu, “Finite Element Modeling of Edge Trimming Fiber Reinforced Plastics,” *J. Manuf. Sci. Eng.*, vol. 124, no. 1, p. 32, 2002.

[20] M. Mahdi and L. Zhang, “A finite element model for the orthogonal cutting of fiber-reinforced composite materials,” *J. Mater. Process. Technol.*, vol. 113, no. 1–3, pp. 373–377, Jun. 2001.

[21] C. C. Chamis, “Simplified composite micromechanics equations of hygral, thermal, and mechanical properties,” 1984.

[22] J. Wang, *Abrasive Technology: Current Development and Applications I: the Third International Conference on Abrasive Technology:(ABTEC’99), Brisbane, Australia, 22-24 November 1999*. World Scientific, 1999.

[23] C. Santiuste, X. Soldani, and M. H. Miguélez, “Machining FEM model of long fiber composites for aeronautical components,” *Compos. Struct.*, vol. 92, no. 3, pp. 691–698, 2010.

[24] P. D. Soden, M. J. Hinton, and A. S. Kaddour, “Lamina properties, lay-up configurations and loading conditions for a range of fibre reinforced composite laminates,” in *Failure Criteria in Fibre-Reinforced-Polymer Composites*, Elsevier, 2004, pp. 30–51.

[25] M. J. Hinton and P. D. Soden, “Predicting failure in composite laminates: the background to the exercise,” *Compos. Sci. Technol.*, vol. 58, no. 7, pp. 1001–1010, 1998.

[26] N. Bhatnagar, D. Nayak, I. Singh, H. Chouhan, and P. Mahajan, “Determination of machining-induced damage characteristics of fiber reinforced plastic composite laminates,” *Mater. Manuf. Process.*, vol. 19, no. 6, pp. 1009–1023, 2004.

[27] L. Lasri, M. Nouari, and M. El Mansori, “Modelling of chip separation in machining unidirectional FRP composites by stiffness degradation concept,” *Compos. Sci. Technol.*, vol. 69, no. 5, pp. 684–692, 2009.

[28] D. Nayak, N. Bhatnagar, and P. Mahajan, “Machining studies of UD-FRP composites part 2: finite element analysis,” *Mach. Sci. Technol.*, vol. 9, no. 4, pp. 503–528, 2005.

[29] G. V. G. Rao, P. Mahajan, and N. Bhatnagar, “Micro-mechanical modeling of machining of FRP composites–Cutting force analysis,” *Compos. Sci. Technol.*, vol. 67, no. 3–4, pp. 579–593, 2007.

[30] C. R. Dandekar and Y. C. Shin, “Multiphase finite element modeling of machining unidirectional composites: prediction of debonding and fiber damage,” *J. Manuf. Sci. Eng.*, vol. 130, no. 5, p. 051016, 2008.

[31] J. Lemaitre and R. Desmorat, *Engineering damage mechanics: ductile, creep, fatigue and brittle failures*. Springer Science & Business Media, 2005.

[32] A. Mkaddem, I. Demirci, and M. El Mansori, "A micro–macro combined approach using FEM for modelling of machining of FRP composites: Cutting forces analysis," *Compos. Sci. Technol.*, vol. 68, no. 15–16, pp. 3123–3127, 2008.

[33] A. U. Manual, "Version 6.12, 2012," *Dassault Systèmes SImulia Corp Provid. RI USA*.

[34] J. D. Littell, C. R. Ruggeri, R. K. Goldberg, G. D. Roberts, W. A. Arnold, and W. K. Binienda, "Measurement of Epoxy Resin Tension, Compression, and Shear Stress–Strain Curves over a Wide Range of Strain Rates Using Small Test Specimens," *J. Aerosp. Eng.*, vol. 21, no. 3, pp. 162–173, Jul. 2008.

[35] P. P. Camanho and C. G. Dávila, "Mixed-mode decohesion finite elements for the simulation of delamination in composite materials," 2002.

[36] R. L. Burden and J. D. Faires, "Numerical analysis. 2001," *BrooksCole USA*, 2001.

[37] Sedighiani, K. and Ayatollahi, M.R., *Finite element analysis; theory and application with ABAQUS*, 3rd ed. Andishesara, 2012.

[38] Y. Zhou, Y. Wang, S. Jeelani, and Y. Xia, "Experimental study on tensile behavior of carbon fiber and carbon fiber reinforced aluminum at different strain rate," *Appl. Compos. Mater.*, vol. 14, no. 1, pp. 17–31, 2007.

[39] H. Hooputra, H. Gese, H. Dell, and H. Werner, "A comprehensive failure model for crashworthiness simulation of aluminium extrusions," *Int. J. Crashworthiness*, vol. 9, no. 5, pp. 449–464, 2004.

[40] A. Hillerborg, M. Modéer, and P.-E. Petersson, "Analysis of crack formation and crack growth in concrete by means of fracture mechanics and finite elements," *Cem. Concr. Res.*, vol. 6, no. 6, pp. 773–781, 1976.

[41] W. M. Lai, D. Rubin, and E. Krempl, *Introduction to continuum mechanics*, 4th ed. Amsterdam ; Boston: Butterworth-Heinemann/Elsevier, 2010.

[42] R. G. Budynas and J. K. Nisbett, *Shigley's mechanical engineering design*, 9th ed. New York: McGraw-Hill, 2011.

[43] G. S. S. Laszlo P. Kollar, *Mechanics of composite structures*. Place of publication not identified: Cambridge University Pres, 2009.

Appendix 1 – ABAQUS Numerical procedure

ABAQUS is one of the most common commercial software used for finite element simulation of cutting process. ABAQUS offers static, quasi-static and dynamic stress analyses. In a static analysis, the sum of all forces is independent of time and equals to zero while in a dynamic analysis, inertia forces due to mass cannot be neglected because acceleration is not zero. Hence, the sum of all forces can be obtained by Newton's second law. A quasi-static analysis is time dependent but assumes that loading is slow enough that inertia forces effect can be neglected. One way to ensure an analysis can be assumed quasi-static is to compare the eigenfrequency of the structure to frequency of loading. Almost any material behavior can be defined by user subroutine (VUMAT). The subroutine acts as an interface, reading data from ABAQUS at the end of each increment, updating the stress-strain responses as well as damage and failure criteria defined and returning the updated values as the input for the next increment to ABAQUS. Basically, two modes of analysis are available in ABAQUS, i.e. Standard and Explicit. ABAQUS Standard is useful for static, low-velocity analyses, where precise stress results are of paramount interest. Assume an engine cover with specific gasket mounted on top of an engine. Frequency and acoustic responses of the pre-stressed cover to engine vibration and noise along with mechanical responses can be obtained in one simulation. ABAQUS/Standard results can be used as initial conditions for Explicit simulations and vice versa. ABAQUS Explicit can be used for analysis in high-speed, nonlinear, transient domains such as impact tests and cutting simulations. Contact nonlinear behavior simulation is one of the most important characteristics of Explicit analysis. [33]

A1.1 Time stability in ABAQUS/Explicit

As mentioned before ABAQUS/Explicit uses central difference operator for integration. The time step needs to be small enough so that the operator is conditionally stable. This is due to the assumption of having the same derivative in a small-time increment. Stability limit for central difference operator is defined by the highest frequency of the system (with no damping) as in Equation 8. [33].

$$\Delta t \leq \frac{2}{w_{max}} \qquad \textbf{Equation 8}$$

When the system includes damping the stable time would be

$$\Delta t \leq \frac{2}{w_{max}}(\sqrt{1-{\varepsilon_{max}}^2}-\varepsilon_{max} \qquad \textbf{Equation 9}$$

Where ε_{max} is the damping fraction in the highest frequency mode. Damping decreases stable time increment. A small amount of damping is introduced in the form of bulk viscosity to control high frequency oscillations.

Highest frequency of the system depends on several interrelated parameters. Hence finding a precise value for it is a difficult task. ABAQUS uses a simple conservative approximation for determining the highest frequency. Instead of considering the whole

model, it computes the highest frequency of each element. The value of the highest frequency for each element would always be higher than model highest frequency [33]. Stable time (depending on elements) can be obtained by knowing the element the dilatational wave speed across any of the elements in the mesh.

$$\Delta t_{stable} \approx \frac{L_{\min}}{c_d} \qquad \textbf{Equation 10}$$

Where $L_{\min}$ is the characteristic length of the element and c_d is the dilatational wave speed. $L_{\min}$ depends on the type of the element. For linear elements, it is equal to the length of the line across the element. For second order elements, it is half of the typical length of the first order elements. For beam, truss, membrane, cohesive and axisymmetric elements the characteristics length is referenced in ABAQUS documentation. [33] Characteristics length of the element is mesh – sensitive because elements with large aspect ratio will behave differently when a crack propagates in different directions. If the elements are too small, computational time will increase dramatically. Keeping the elements large may not give the best realistic results. So, finding the right size of the element is important. ABAQUS provides a list of 10 elements with the lowest stable time limit to prevent the stability limit problem. It might be a better idea to re-mesh the model if the stable time is too small knowing that the physical results can be at stake by increasing the element size. [33] c_d is a property of the material. Two kinds of waves in a homogeneous material can be defined; dilatational (pressure) waves (c_d) and shear (secondary) waves (c_s). The velocity of each wave is obtained by [33].

$$c_d = \sqrt{\frac{E}{\rho}} \qquad \textbf{Equation 11}$$

$$c_s = \sqrt{\frac{G}{\rho}} \qquad \textbf{Equation 12}$$

Where E, ρ and G are, the Young modulus, density and shear modulus of the isotropic material. Shear waves move perpendicular to the wave propagation direction. Stable time limit calculator of ABAQUS uses dilatational (pressure) wave speed not shear. Therefore, the stiffer the material the higher the wave speed and the smaller the stability time limit.

A1.2 Mass scaling for controlling time stability

Stable time increment depends on the density. Small density increases dilatational wave speed in the element and consequently decreases the stable time limit significantly. Thus, for some analyses it is beneficial to use mass scaling to make them more efficient. For example, to mesh complex geometries, very small elements are required to cover complicated regions. These small elements would reduce the stable time. Usually the number of these elements is small. By increasing the mass of these elements, the minimum stable time would increase without influencing global dynamic behavior of the model. [33]

A1.3 ABAQUS contact enforcement algorithms

ABAQUS uses two type of contact enforcement methods [33].

- Kinematic
- Penalty

For pair contacts, where master and slave surfaces are defined, one can choose between kinematic and penalty algorithms for contact enforcement. However, the general contact in ABAQUS uses Penalty approach as default.

A1.3.1 Kinematic enforcement of contact conditions

The following basic procedure explain how ABAQUS enforces contact conditions by kinematic method. First analysis is advanced without considering contact conditions. Then, the distance that the slave nodes penetrated into the master surface is recorded. Required force to resist the penetration is then calculated using the nodal mass, depth of penetration and time increment. Then, the sum of resisting force for all slave nodes is distributed on the master surface nodes. The mass of contacting slave nodes (some of the slave nodes might not even contact the master surface in that time step) is added to the mass of master nodes. Acceleration correction for master nodes is then calculated and at the final step acceleration correction for slave nodes is corrected [33]. Penetration of master node into slave surface is shown in Figure 45.

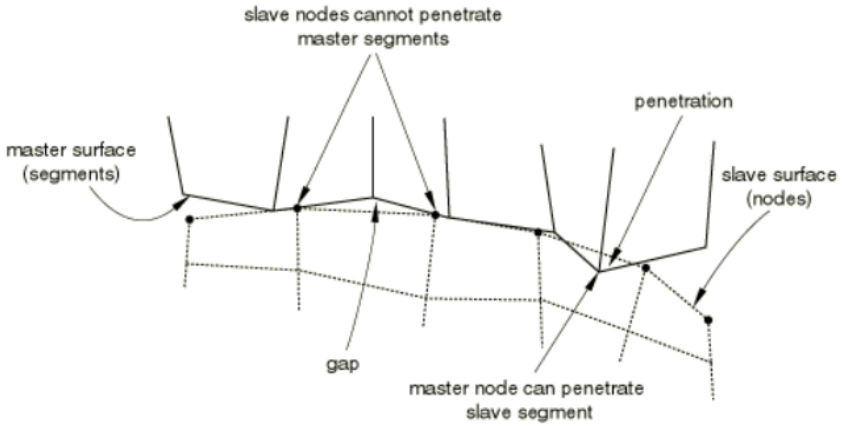

Figure 45 - Master surface penetration into slave surface [33]

A1.3.2 Penalty enforcement of contact conditions

Penalty algorithm is helpful to simulate more general contact types such as multiple contacts per node, contact between rigid bodies. The following basic procedure explains how ABAQUS uses penalty algorithm to enforce contact conditions. The resisting force as a function of penetration depth, same as kinematic algorithm, is applied to the slave nodes to oppose penetration. Also, equal and opposite forces are applied to the master nodes at penetration points. The contact forces at penetration points are then distributed on the master nodes being penetrated. It should be noted that penetration points might differ from penetrated nodes. Distribution of the resisting forces at penetration points over the master nodes depends on the type of master surface contact. Penalty algorithm includes node-into-face, node-into-analytical rigid surface and node-into-edge

penetrations. In ABAQUS, general contact always uses the penalty algorithm while for contact pairs user can choose between kinematic and penalty algorithms. Since penalty algorithm adds stiffness to the model, stable time increment can be affected. [33]

A1.4 Ductile damage modeling of polymeric matrix

Two types of damage mechanics are considered to occur during fracture mechanism of the matrix material in this study;

a) nucleation, growth and coalescence of voids
b) shear band (strain) localization

Progressive damage model for this material can be explained by the help of Figure 46. Undamaged constitutive behavior can be seen up to damage initiation point, A, where damage variable, D, equals to zero the. Elastic-plastic behavior of the epoxy material with isotropic hardening is defined in this zone. Zone A-B is the damaged evolution according to the specified damage response. At point B, elements are removed and will no longer carry the load. Damage manifests itself in two ways; degradation of stiffness (young modulus) and softening of the yield stress. The former can be noticed in fig by the smaller slope of the isotropic hardening line at point C. As can obviously been seen, the yield stress at point C is smaller than yield stress at damage initiation point A. Here $\bar{\sigma}$ represents the undamaged stress.

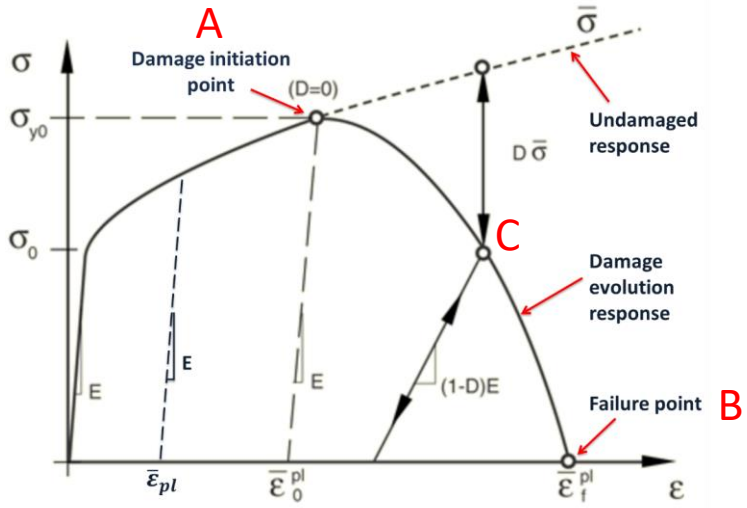

Figure 46 - progressive damage demonstration for elastic-plastic with isotropic hardening [33]

σ_{y0} and $\bar{\varepsilon}_0^{pl}$ are yield stress and equivalent plastic strain at the onset of damage, $\bar{\varepsilon}_f^{pl}$ is the equivalent plastic strain at failure point of the material, where D equals to unity. respectively. It should be noted that σ_{yo} is different than the Von Mises yield strength of the material. It lies in the plastic region of the stress-strain curve.

A1.4.1 Damage initiation

ABAQUS uses equivalent plastic strain $\bar{\varepsilon}^{pl}$ to define the initiation point of the damage criterion. As mentioned before, two damage mechanisms are considered for matrix in this study.

A1.4.1.1 Ductile damage initiation

In ductile damage occurs due to nucleation and growth of voids (Figure 47). Equivalent plastic strain in the ductile damage model is a function of stress triaxiality and strain rate [33].

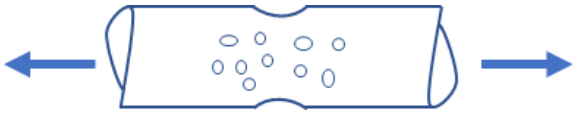

Figure 47 – ductile damage initiation due to nucleation and growth of voids

Stress triaxiality is defined the ratio of the hydrostatic pressure stress to Von Mises equivalent stress. for more information on stress triaxiality refer to Appendix 2. Equation 13 defines the equivalent plastic strain as a function of stress triaxiality in the ductile damage criterion in ABAQUS [33].

$$\bar{\varepsilon}^{pl}_{ductile} = \frac{\varepsilon_T^{+}\sinh[k_0(\eta^{-}-\eta)] + \varepsilon_T^{-}\sinh[k_0(\eta-\eta^{+})]}{\sinh[k_0(\eta^{-}-\eta^{+})]} \qquad \textbf{Equation 13}$$

Where,

η: stress triaxiality

η^{+}: stress triaxiality in equibiaxial tensile deformation (2/3 for isotropic materials)

η^{-}: stress triaxiality in equibiaxial compressive deformation (-2/3 for isotropic materials)

ε_T^{+}: equivalent plastic strain at ductile damage initiation for equibiaxial tensile deformation

ε_T^{-} : equivalent plastic strain at ductile damage initiation for equibiaxial compressive deformation.

k_0 : constant[1].

It should be noted that three material parameters, ε_T^{+}, ε_T^{-} and k_0 are dependent on strain rate and obtained experimentally. Having these three parameters, one can obtain a tabular data on equivalent plastic strain at different triaxiality values. In ABAQUS the onset of the ductile damage happens when the condition in Equation 14 is satisfied [33].

[1] Stress triaxiality definition in ABAQUS differs from one defined in Hooputra et al. [39] by a factor of 1/3. Hence, value of k_0 in Equation 20 is three times the value used by Hooputra et al [39].

$$w_{ductile} = \int \frac{d\bar{\varepsilon}^{pl}}{\varepsilon^{pl}_{ductile}(\eta, \dot{\varepsilon}^{pl}_{d})} = 1 \qquad \textbf{Equation 14}$$

$w_{ductile}$ is a state variable that increases monotonically with plastic deformation [33].

A1.4.1.2 Shear damage initiation

Shear band localization (Figure 48) can be modeled using the shear damage criterion in ABAQUS.

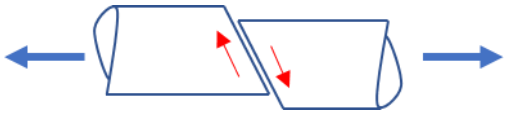

Figure 48 - shear damage initiation due to shear band localization

Similar to ductile damage criterion, this model uses equivalent plastic strain. However, here it is a function of shear stress ratio and strain rate. Equation 15 represents the shear stress ratio used in ABAQUS. [33]

$$\theta_s = \frac{q + k_s p}{\tau_{\max}} \qquad \textbf{Equation 15}$$

Where,

θ_s is the shear stress ratio

q is the Von Mises equivalent stress

p is the hydrostatic (pressure) stress and

k_s is a material constant

In ABAQUS the onset of the shear damage happens when the condition in Equation 16 is satisfied. [33]

$$w_{shear} = \int \frac{d\bar{\varepsilon}^{pl}}{\varepsilon^{pl}_{shear}(\theta_s, \dot{\varepsilon}^{pl}_{s})} = 1 \qquad \textbf{Equation 16}$$

w_{shear} is a state variable that increases monotonically with plastic deformation [33].

A1.4.2 Damage evolution

Scalar formulation that ABAQUS uses to implement material degradation is given by Equation 17.

$$\sigma = (1 - D)\bar{\sigma} \qquad \textbf{Equation 17}$$

Where $\bar{\sigma}$ represents the stress due to undamaged response. The rate of degradation of the material can be specified by different approaches in ABAQUS. Instead of equivalent

plastic failure strain, equivalent plastic displacement ($\bar{u}^{pl}$) or fracture energy (G_f) values at failure are used to define damage evolution response. [33] This is to reduce mesh-dependency of the formulation. Linear, exponential and tabular approaches can be used to define softening of the material during displacement-based damage evolution. Figure 49 shows the difference between these three methods. In the present work, linear degradation approach is used by defining the displacement at failure for the matrix material.

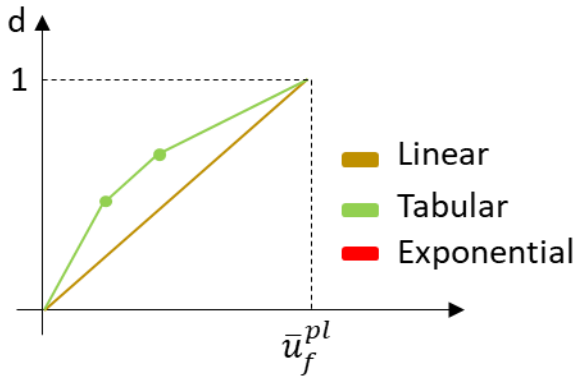

Figure 49 – displacement-based damage evolution approach

ABAQUS uses Hillerborg's 1976 [40] fracture energy proposal to specify damage behavior of the material. Hillerborg's fracture energy is given by Equation 18. It should be noted that tabular approach does not exist for energy-based damage evolution response (Figure 50).

$$G_f = \int_{\bar{\varepsilon}_0^{pl}}^{\bar{\varepsilon}_f^{pl}} L\sigma_y d\bar{\varepsilon}^{pl} = \int_0^{\bar{u}_f^{pl}} \sigma_y d\bar{u}^{pl} \qquad \textbf{Equation 18}$$

Where,

$$\bar{u}^{pl} = L\bar{\varepsilon}^{pl} \qquad \textbf{Equation 19}$$

L is the characteristic length of the element which depends on the geometry of the element.

$\bar{\varepsilon}_f^{pl}$ is strain at failure

$\bar{u}_f^{pl}$ is displacement at failure

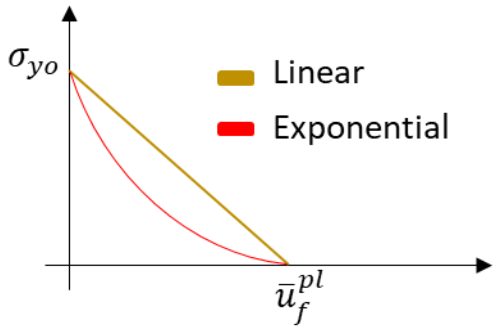

Figure 50 - energy-based damage evolution approach

Damage evolution response is also capable of capturing the effects of different damage modes at the same time. This means damage behavior in three different planes (normal, shear 1 and shear 2) can be implemented in ABAQUS. Even the level of contribution of each damage mechanism can be defined. The multiplicative effect of damage variable can be obtained using Equation 20. The overall damage variable, D, is the maximum of d_{mult} and each damage variables. In the present work, only normal damage mode is considered.

$$d_{mult} = 1 - \prod_{k \in N_{mult}} (1 - d_k) \qquad \textbf{Equation 20}$$

Appendix 2 – Stress Triaxiality

Cauchy stress tensor consists of nine components that completely define the state of stress at a material point in a deformed state, placement or configuration [41].

$$\sigma = \begin{bmatrix} \sigma_x & \tau_{xy} & \tau_{xz} \\ \tau_{yx} & \sigma_y & \tau_{yz} \\ \tau_{zx} & \tau_{zy} & \sigma_z \end{bmatrix} \qquad \textbf{Equation 21}$$

According to the principle of linear conservation of energy, in the static equilibrium condition, components of Cauchy stress tensor are equal to zero. On the other hand, the principle of angular momentum conservation, the summation of moments in an arbitrary point is zero. Hence, the stress tensor is symmetric. In a 3D generic stress condition, the stress tensor has six independent components.

Stress, and similarly strain tensors can be decomposed into volumetric (hydrostatic) and deviatoric stresses/strains. The volumetric strain purely corresponds to a change in the volume of the object maintaining the overall shape of it. This means without any angular deformations, like scaling an object. In contrast, deviatoric strain corresponds to the shearing and distortion effects observed.

The first law of the thermodynamics states that energy is neither created nor destroyed, only converted from one form to another. When a mechanical force is applied to an object, some work is being done. The stored energy, strain energy of the body, for a homogeneous material is defined as

$$U = \frac{1}{2}\sigma\varepsilon \qquad \textbf{Equation 22}$$

This strain energy in a solid may not be distributed uniformly throughout the solid. So, the concept of strain energy density introduced, which is strain energy per unit volume. The total strain energy is consisted of volumetric energy (changing the volume of the material) and deviatoric (distortion) energy related to shear deformations (changing the shape of the material). [42]

A2.1 Distortion strain energy

In experiments, yield strengths of ductile materials under hydrostatic stress conditions (equal principal stress) was observed to be greatly higher than the values obtained by simple tension stress. Therefore, yielding of these materials was not only because of the simple tension or compression but also due to angular distortion of the stressed element. Each 3D stress state for each element can be characterized by principle stresses in 3 directions, σ_1 , σ_2 and σ_3. This state is to be called from now on as triaxial situation. Principal strains in this case are [42].

$$\varepsilon_1 = \frac{1}{E}[\sigma_1 - \nu(\sigma_2 + \sigma_3)]$$
$$\varepsilon_2 = \frac{1}{E}[\sigma_2 - \nu(\sigma_1 + \sigma_3)] \quad \textbf{Equation 23}$$
$$\varepsilon_3 = \frac{1}{E}[\sigma_3 - \nu(\sigma_1 + \sigma_2)]$$

The total strain energy per unit volume of material at principal directions is defined as

$$U = \frac{1}{2}\sigma_1\varepsilon_1 + \frac{1}{2}\sigma_2\varepsilon_2 + \frac{1}{2}\sigma_3\varepsilon_3 \quad \textbf{Equation 24}$$

Substituting ε_1, ε_2, and ε_3 from Equation 23 in Equation 24, strain energy density can be defined as

$$U = \frac{1}{2E}[(\sigma_1^2 + \sigma_2^2 + \sigma_3^2 - 2\nu(\sigma_1\sigma_2 + \sigma_2\sigma_3 + \sigma_1\sigma_3)] \quad \textbf{Equation 25}$$

The element's stresses at principal directions can be consisted of two types of stresses: hydrostatic normal stresses and distortion stresses. In other words, hydrostatic part of the principle stresses corresponds to three equal stresses each equal to the average of the three principle stresses) and distortion stresses correspond to the rest of the principle stresses value.

Hydrostatic pressure state for producing only the volume change, happens when the stresses in 3 directions are equal to the average of the three principal stresses:

$$\sigma_{ave} = \frac{\sigma_1 + \sigma_2 + \sigma_3}{3} \quad \textbf{Equation 26}$$

Hydrostatic strain is the average volumetric strain:

$$\varepsilon_h = \frac{\varepsilon_{vol}}{3} = \frac{\varepsilon_1 + \varepsilon_2 + \varepsilon_3}{3} \quad \textbf{Equation 27}$$

Bulk modulus is the ratio of the average pressure stress to volumetric strain

$$K = \frac{\sigma_{ave}}{\varepsilon_h} \quad \textbf{Equation 28}$$

For an isotropic material elastic, shear and bulk modulus are not independent and are related via Equation 29 [42].

$$2G(1+\nu) = E = 3K(1-2\nu) \qquad \textbf{Equation 29}$$

To obtain hydrostatic energy, one can substitute the three principal stresses in Equation 25 with σ_{ave}:

$$\begin{aligned} U_{vol} &= \frac{1}{2E}[(\sigma_{ave}^2 + \sigma_{ave}^2 + \sigma_{ave}^2 - 2\nu(\sigma_{ave}\sigma_{ave} + \sigma_{ave}\sigma_{ave} + \sigma_{ave}\sigma_{ave})] \\ &= \frac{1}{2E}[3\sigma_{ave}^2 - 2\nu(3\sigma_{ave}^2)] \\ &= \frac{3\sigma_{ave}^2(1-2\nu)}{2E} \end{aligned} \qquad \textbf{Equation 30}$$

Hydrostatic energy can be expressed in terms of principal stresses by squaring Equation 26 and substituting the result in Equation 30.

$$U_{vol} = \frac{1-2\nu}{6E}[(\sigma_1^2 + \sigma_2^2 + \sigma_3^2 - 2\nu(\sigma_1\sigma_2 + \sigma_2\sigma_3 + \sigma_1\sigma_3)] \qquad \textbf{Equation 31}$$

Now distortion energy can be computed by subtracting Equation 31 from Equation 25.

$$U_{dist.} = U - U_{vol} = \frac{1+\nu}{3E}\left[\frac{(\sigma_1^2 - \sigma_2^2) + (\sigma_2^2 - \sigma_3^2) + (\sigma_3^2 - \sigma_1^2)}{2}\right] \qquad \textbf{Equation 32}$$

A2.2 Von mises Equivalent stress

Von mises equivalent stress is a representative of stress components in the deviatoric stress tensor or distortion energy. According to the Von Mises's theory, a ductile solid will yield when the distortion energy density equals the yield strength of that material in the simple tensile test. [42] In a simple tensile test, $\sigma_1 = \sigma_y$ and $\sigma_2 = \sigma_3 = 0$. Hence, the strain energy is.

$$U_{dist.} = \frac{1+\nu}{3E}\sigma_y^2 \qquad \textbf{Equation 33}$$

When Yielding occurs in any material, the distortion strain energy per unit volume at the point of failure equals or exceeds the distortion strain energy per unit volume when yielding occurs in the tension test specimen. Thus,

$$\frac{1+\nu}{3E}\left[\frac{(\sigma_1^2 - \sigma_2^2) + (\sigma_2^2 - \sigma_3^2) + (\sigma_3^2 - \sigma_1^2)}{2}\right] = \frac{1+\nu}{3E}\sigma_y^2 \qquad \textbf{Equation 34}$$

Von Mises equivalent stress then can be defined as

$$\sigma_y = \left[\frac{(\sigma_1^2 - \sigma_2^2) + (\sigma_2^2 - \sigma_3^2) + (\sigma_3^2 - \sigma_1^2)}{2} \right]^{\frac{1}{2}}$$ **Equation 35**

A2.3 Stress Triaxiality

Stress Triaxially is defined as the ratio of the hydrostatic pressure stress (mean stress) to Von Mises equivalent stress. [33]

$$\eta = \frac{-p}{q} = \frac{-\sigma_{ave}}{\sigma_y} = \frac{-\frac{1}{3}(\sigma_1 + \sigma_2 + \sigma_3)}{\frac{1}{\sqrt{2}}\sqrt{(\sigma_1 - \sigma_2)^2 + (\sigma_2 - \sigma_3)^2 + (\sigma_3 - \sigma_1)^2}}$$ **Equation 36**

Where σ_1 , σ_2 and σ_3 are the first, second and third principal stresses, respectively.

Appendix 3 – Transformation

A3.1 Vector transformation

Vector $\vec{u}$ is real and independent of the coordination system used to define it (Figure 51). [41]

$$\vec{u} = u_x\vec{i} + u_y\vec{j} + u_z\vec{k} = u'_x\vec{i}' + u'_y\vec{j}' + u_z\vec{k}' \qquad \textbf{Equation 37}$$

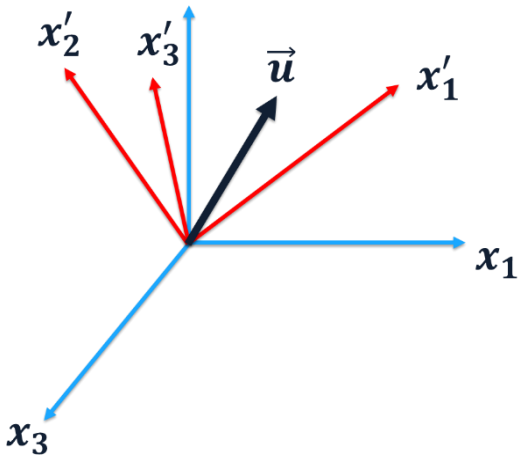

Figure 51 - coordination system rotation vectors

Inner product of vector **u** by unit vector in x direction **i** will produce

$$u.\vec{j} = u'_x(\vec{i}'.\vec{i}) + u'_y(\vec{j}'.\vec{i}) + u_z(\vec{k}'.\vec{i}) \qquad \textbf{Equation 38}$$

$$u_x = \begin{bmatrix}(\vec{i}'.\vec{i}) & (\vec{j}'.\vec{i}) & (\vec{k}'.\vec{i})\end{bmatrix}\begin{bmatrix}u_x'\\u_y'\\u_z'\end{bmatrix} \qquad \textbf{Equation 39}$$

Similarly,

$$u_y = \begin{bmatrix}(\vec{i}'.\vec{j}) & (\vec{j}'.\vec{j}) & (\vec{k}'.\vec{j})\end{bmatrix}\begin{bmatrix}u_x'\\u_y'\\u_z'\end{bmatrix} \qquad \textbf{Equation 40}$$

$$u_z = \begin{bmatrix}(\vec{i}'.\vec{k}) & (\vec{j}'.\vec{k}) & (\vec{k}'.\vec{k})\end{bmatrix}\begin{bmatrix}u_x'\\u_y'\\u_z'\end{bmatrix} \qquad \textbf{Equation 41}$$

Or in the matrix form

$$\begin{bmatrix} u_x \\ u_y \\ u_z \end{bmatrix} = \begin{bmatrix} (\boldsymbol{i}'.\boldsymbol{i}) & (\boldsymbol{j}'.\boldsymbol{i}) & (\boldsymbol{k}'.\boldsymbol{i}) \\ (\boldsymbol{i}'.\boldsymbol{j}) & (\boldsymbol{j}'.\boldsymbol{j}) & (\boldsymbol{k}'.\boldsymbol{j}) \\ (\boldsymbol{i}'.\boldsymbol{k}) & (\boldsymbol{j}'.\boldsymbol{k}) & (\boldsymbol{k}'.\boldsymbol{k}) \end{bmatrix} \begin{bmatrix} u'_x \\ u'_y \\ u'_z \end{bmatrix} \qquad \textbf{Equation 42}$$

Entries of the rotation matrix are referred to as directional cosines. In general

$$\boldsymbol{e}_i = Q_{ij}\boldsymbol{e}'_j, \quad \boldsymbol{e}'_i = Q_{ji}\boldsymbol{e}_j \qquad \textbf{Equation 43}$$

A3.2 Tensor transformation

As with vectors, components of a second order tensor (stress or strain tensor for example) can be found after rotation of the coordination system in a new coordination system

$$\sigma_{ij} = Q_{ip}Q_{jq}\sigma'_{pq}, \qquad \varepsilon'_{ij} = Q_{pi}Q_{qj}\varepsilon_{pq} \qquad \textbf{Equation 44}$$

Or in matrix form:

$$[T'] = [Q^T][T][Q] \qquad [T] = [Q][T'][Q^T] \qquad \textbf{Equation 45}$$

Appendix 4 – Transversely Isotropic Material

General Hook's law for linear elastic materials states that

$$\begin{bmatrix}\sigma_1\\ \sigma_2\\ \sigma_3\\ \sigma_4\\ \sigma_5\\ \sigma_6\end{bmatrix} = \begin{bmatrix}c_{11} & c_{12} & c_{13} & c_{14} & c_{15} & c_{16}\\ c_{21} & c_{22} & c_{23} & c_{24} & c_{25} & c_{26}\\ c_{31} & c_{32} & c_{33} & c_{34} & c_{35} & c_{36}\\ c_{41} & c_{42} & c_{43} & c_{44} & c_{45} & c_{46}\\ c_{51} & c_{52} & c_{53} & c_{54} & c_{55} & c_{56}\\ c_{61} & c_{62} & c_{63} & c_{64} & c_{65} & c_{66}\end{bmatrix} \cdot \begin{bmatrix}\varepsilon_1\\ \varepsilon_2\\ \varepsilon_3\\ \varepsilon_4\\ \varepsilon_5\\ \varepsilon_6\end{bmatrix} \quad \textbf{Equation 46}$$

$$\sigma_i = c_{ij}.\varepsilon_j \quad \textbf{Equation 47}$$

Where,

$$\begin{aligned}\sigma_1 &= \sigma_{11}, & \varepsilon_1 &= \varepsilon_{11}\\ \sigma_2 &= \sigma_{22}, & \varepsilon_2 &= \varepsilon_{22}\\ \sigma_3 &= \sigma_{33}, & \varepsilon_3 &= \varepsilon_{33}\\ \sigma_4 &= \sigma_{23}, & \varepsilon_4 &= 2\varepsilon_{23}\\ \sigma_5 &= \sigma_{13}, & \varepsilon_5 &= 2\varepsilon_{13}\\ \sigma_6 &= \sigma_{12}, & \varepsilon_6 &= 2\varepsilon_{12}\end{aligned}$$

Stress and strain components are in the form of normal and shear. C_{ij}'s are material constants (stiffness) and can be obtained experimentally. As discussed in Appendix, the stiffness matrix must be symmetric according to angular moment conservation law. So, there are only 21 independent elastic constants in the case of anisotropic materials which is the most general case [43].

A4.1 Material symmetry

A4.1.1 Monoclinic materials

These materials have only one plane of symmetry. [43] Let's consider plane (x_2=0) as the plane of symmetry as shown in Figure 52. Change of axes can be interpreted as:

$$x_1' = x_1,$$
$$x_2' = x_2$$
$$x_3' = -x_3$$

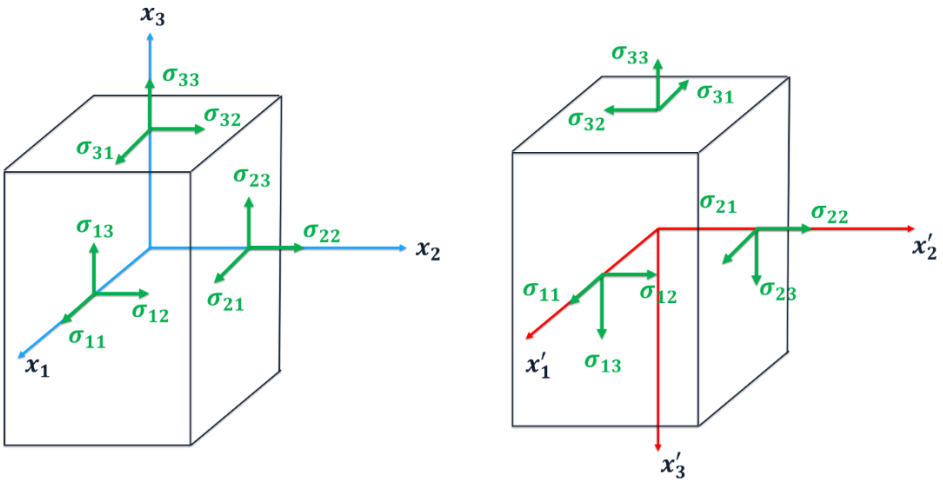

Figure 52 - elemental stresses for a monoclinic material [symmetry plane 1-2 normal vector x3]

Mathematically the following equations state the transformation matrix between the old and new coordination systems.

$$Q_{ij} = \frac{\partial x'_i}{\partial x_j} = \begin{cases} \delta_{ij}, & j = 1,2 \\ -\delta_{i2}, & j = 3 \end{cases}$$ **Equation 48**

Where δ_{ij} is the Kronecker delta. ($Q_{11}=Q_{22}=1$, $Q_{33}=-1$)

In appendix 3, it was shown that tensor (stress and strain) transformation obeys the following law:

$$\sigma_{ij} = Q_{ip}Q_{jq}\sigma'_{pq}, \qquad \varepsilon'_{ij} = Q_{pi}Q_{qj}\varepsilon_{pq}$$

For Monoclinic materials stresses in two coordination systems can be related to each other as follows:

$$\sigma'_{11} = \sigma_{11}, \qquad \sigma'_{23} = -\sigma_{23}$$
$$\sigma'_{22} = \sigma_{22}, \qquad \sigma'_{13} = -\sigma_{13}$$
$$\sigma'_{33} = \sigma_{33}, \qquad \sigma'_{12} = \sigma_{12}$$

Similarly, for strains:

$$\varepsilon'_{11} = \varepsilon_{11}, \qquad \varepsilon'_{23} = -\varepsilon_{23}$$
$$\varepsilon'_{22} = \varepsilon_{22}, \qquad \varepsilon'_{13} = -\varepsilon_{13}$$
$$\varepsilon'_{33} = \varepsilon_{33}, \qquad \varepsilon'_{12} = \varepsilon_{12}$$

Here, ε_{22}, ε_{13} and ε_{23} are calculated:

$$\varepsilon'_{22} = Q_{p2}Q_{q2}\varepsilon_{pq}$$

$$P=1,\quad \begin{cases} q=1, & Q_{12}Q_{12}\varepsilon_{11}=\mathbf{0} \\ q=2, & Q_{12}Q_{22}\varepsilon_{12}=\mathbf{0} \\ q=3, & Q_{12}Q_{32}\varepsilon_{13}=\mathbf{0} \end{cases}$$

$$P=2,\quad \begin{cases} q=1, & Q_{22}Q_{12}\varepsilon_{21}=\mathbf{0} \\ q=2, & Q_{22}Q_{22}\varepsilon_{22}=(\mathbf{1})\times(\mathbf{1})\times\boldsymbol{\varepsilon_{22}}=\boldsymbol{\varepsilon_{22}} \\ q=3, & Q_{22}Q_{32}\varepsilon_{23}=\mathbf{0} \end{cases}$$

$$P=3,\quad \begin{cases} q=1, & Q_{32}Q_{12}\varepsilon_{31}=\mathbf{0} \\ q=2, & Q_{32}Q_{22}\varepsilon_{32}=\mathbf{0} \\ q=3, & Q_{32}Q_{32}\varepsilon_{33}=\mathbf{0} \end{cases}$$

$$\rightarrow \boldsymbol{\varepsilon'_{22}=\varepsilon_{22}}$$

$$\varepsilon'_{13}=Q_{p1}Q_{q3}\varepsilon_{pq}$$

$$P=1,\quad \begin{cases} q=1, & Q_{11}Q_{13}\varepsilon_{11}=\mathbf{0} \\ q=2, & Q_{11}Q_{23}\varepsilon_{12}=\mathbf{0} \\ q=3, & Q_{11}Q_{33}\varepsilon_{13}=(\mathbf{1})\times(\mathbf{-1})\times\varepsilon_{13}=\boldsymbol{-\varepsilon_{13}} \end{cases}$$

$$P=2,\quad \begin{cases} q=1, & Q_{21}Q_{12}\varepsilon_{21}=\mathbf{0} \\ q=2, & Q_{21}Q_{22}\varepsilon_{22}=\mathbf{0} \\ q=3, & Q_{21}Q_{32}\varepsilon_{23}=\mathbf{0} \end{cases}$$

$$P=3,\quad \begin{cases} q=1, & Q_{31}Q_{12}\varepsilon_{31}=\mathbf{0} \\ q=2, & Q_{31}Q_{22}\varepsilon_{32}=\mathbf{0} \\ q=3, & Q_{31}Q_{32}\varepsilon_{33}=\mathbf{0} \end{cases}$$

$$\rightarrow \boldsymbol{\varepsilon'_{13}=-\varepsilon_{13}}$$

$$\varepsilon'_{23}=Q_{p2}Q_{q3}\varepsilon_{pq}$$

$$P=1,\quad \begin{cases} q=1, & Q_{12}Q_{13}\varepsilon_{11}=\mathbf{0} \\ q=2, & Q_{12}Q_{23}\varepsilon_{12}=\mathbf{0} \\ q=3, & Q_{12}Q_{33}\varepsilon_{13}=\mathbf{0} \end{cases}$$

$$P=2,\quad \begin{cases} q=1, & Q_{22}Q_{13}\varepsilon_{21}=\mathbf{0} \\ q=2, & Q_{22}Q_{23}\varepsilon_{22}=\mathbf{0} \\ q=3, & Q_{22}Q_{33}\varepsilon_{23}=(\mathbf{-1})\times(\mathbf{1})=\boldsymbol{-\varepsilon_{23}} \end{cases}$$

$$P=3,\quad \begin{cases} q=1, & Q_{32}Q_{13}\varepsilon_{31}=\mathbf{0} \\ q=2, & Q_{32}Q_{23}\varepsilon_{32}=\mathbf{0} \\ q=3, & Q_{32}Q_{33}\varepsilon_{33}=\mathbf{0} \end{cases}$$

$$\rightarrow \boldsymbol{\varepsilon'_{23}=-\varepsilon_{23}}$$

Now using the stiffness matrix, in general Hook's law, and stress and strain relations above for monoclinic materials we can write:

$$\sigma'_{11} = \sigma_{11}$$

$$c'_{11}\varepsilon'_1 + c'_{12}\varepsilon'_2 + c'_{13}\varepsilon'_3 + c'_{14}\varepsilon'_4 + c'_{15}\varepsilon'_5 + c'_{16}\varepsilon'_6 = c_{11}\varepsilon_1 + c_{12}\varepsilon_2 + c_{13}\varepsilon_3 + c_{14}\varepsilon_4 + c_{15}\varepsilon_5 + c_{16}\varepsilon_6$$

Using strain equations

$$-c'_{14}\varepsilon_4 - c'_{15}\varepsilon_5 = c_{14}\varepsilon_4 + c_{15}\varepsilon_5$$

Since $c_{ij} = c'_{ij}$, then:

$$c_{14} = c_{15} = 0$$

Similarly,

$$\sigma_{22} = \sigma'_{22}, \text{ gives: } c_{24} = c_{25} = 0$$
$$\sigma_{33} = \sigma'_{33}, \text{ gives: } c_{34} = c_{35} = 0$$
$$\sigma_{23} = -\sigma'_{23}, \text{ gives: } c_{46} = 0$$
$$\sigma_{13} = -\sigma'_{13}, \text{ gives: } c_{56} = 0$$

Hence the stiffness matrix for a monoclinic material will be:

$$c_{ij_{monoclinic}} = \begin{bmatrix} c_{11} & c_{12} & c_{13} & 0 & 0 & c_{16} \\ c_{21} & c_{22} & c_{23} & 0 & 0 & c_{26} \\ c_{31} & c_{32} & c_{33} & 0 & 0 & c_{36} \\ 0 & 0 & 0 & c_{44} & c_{45} & 0 \\ 0 & 0 & 0 & c_{54} & c_{55} & 0 \\ c_{61} & c_{62} & c_{63} & 0 & 0 & c_{66} \end{bmatrix} \quad \textbf{Equation 49}$$

The number of independent components in the stiffness matrix reduces to only 13 versus 21 of anisotropic materials.

A4.1.2 Orthotropic materials

An orthotropic material has three orthogonal planes of symmetry as can be seen in Figure 53. CFRP UD Lamina can be assumed as an orthotropic material. It is clear that if any two orthogonal planes are planes of material symmetry the third mutually orthogonal plane has to be plane to material symmetry.a

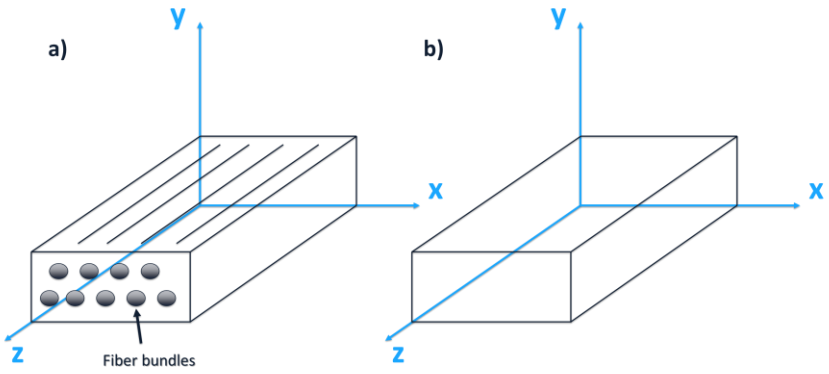

Figure 53 - orthotropic material a) microstructure b) macro structure

The CFRP lamina shown in figure above, possess stronger properties in the z direction compared to the other two directions. *x*, *y* and *z* axes define the orientation of the material.

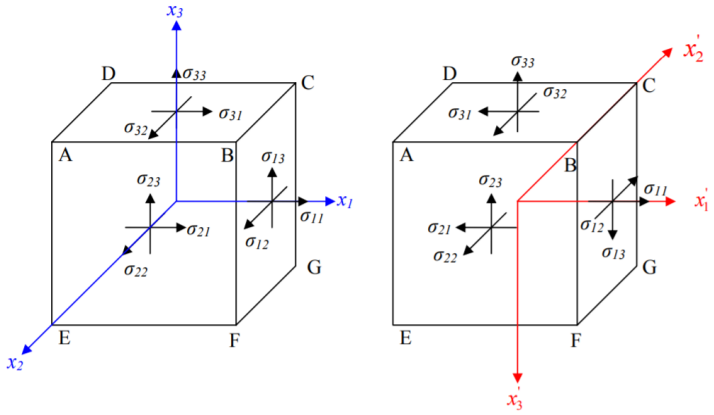

Figure 54 - elemental stresses for an orthotropic material [symmetry planes 1-2 and 1-3 with normal vectors x3 and x2]

With same principal used for monoclinic materials, it can be shown that the stiffness matrix of orthotropic materials is as follows [43]

$$C_{ij}{}_{orthotropic} = \begin{bmatrix} C_{11} & C_{12} & C_{13} & 0 & 0 & 0 \\ C_{21} & C_{22} & C_{23} & 0 & 0 & 0 \\ C_{31} & C_{32} & C_{33} & 0 & 0 & 0 \\ 0 & 0 & 0 & C_{44} & 0 & 0 \\ 0 & 0 & 0 & 0 & C_{55} & 0 \\ 0 & 0 & 0 & 0 & 0 & C_{66} \end{bmatrix} \quad \textbf{Equation 50}$$

The End